

THESIS FOR THE DEGREE OF DOCTOR OF PHILOSOPHY

Tailored process gases for laser powder bed fusion

CAMILLE PAUZON

Department of Industrial and Materials Science

CHALMERS UNIVERSITY OF TECHNOLOGY

Gothenburg, Sweden 2021

Tailored process gases for laser powder bed fusion

Camille Pauzon
ISBN 978-91-7905-432-8

© Camille Pauzon, 2021

Doctoral thesis at Chalmers University of Technology
New serial no: 4899
ISSN 0346-718X

Department of Industrial and Materials Science
Chalmers University of Technology
SE-412 96 Gothenburg
Sweden
Telephone + 46 (0)31-772 1000
URL: www.chalmers.se

Printed by Chalmers Reproservice
Gothenburg, Sweden 2021

Tailored process gases for laser powder bed fusion

CAMILLE PAUZON

Department of Industrial and Materials Science

Chalmers University of Technology

Abstract

Metal laser powder bed fusion (L-PBF) allows for production of complex components using the energy from a laser to locally melt micron-sized powder following a layer-wise approach. Considerable scientific efforts are focused on addressing the influence of the process parameters on the melting stability and the control of material properties, while developing necessary monitoring and characterization tools. The importance of the process atmosphere has largely been undermined in favour of first order parameters connected to the laser scanning. The role of the atmosphere has been limited to the reduction of the operating residual oxygen level down to typically 1000 ppm. This thesis focuses on providing knowledge on the influence of the process atmosphere on the laser – metal powder interaction during L-PBF and the resulting properties of the built material in terms of generated defects, microstructure and mechanical properties. Different purities and compositions of generated atmospheres have been investigated to manufacture the most used materials in the field, namely 316L stainless steel, Alloy 718 and Ti-6Al-4V. The scope of process gases was extended from the traditionally employed argon to also include nitrogen, helium and mixtures of argon and helium. Purities from the typical 1000 ppm O₂ threshold down to a few ppm were achieved using external monitoring of the atmosphere on both industrial- and laboratory-scale production machines.

The investigated materials displayed different sensitivities to the atmosphere composition. 316L stainless steel had limited differences in terms of composition and strength when processed with high purity argon or nitrogen. Only processing with a built-in nitrogen generator, with which the process starts as soon as 10000 ppm residual O₂ is reached, led to the increased oxidation of spatter particles and the appearance of large lack-of-fusion defects. A reduction in residual oxygen down to few ppm allowed to significantly hinder the development of thick Cr- and Al-rich particulate oxides on the surface of Alloy 718 spatter particles exposed to the L-PBF environment. In addition, Ti-6Al-4V had the highest sensitivity to the presence of impurities with significant oxygen and nitrogen pick-ups leading to embrittlement. This could be partially mitigated by limiting heat accumulation with longer interlayer time at the expense of productivity or by decreasing the oxygen level in the build chamber to below 100 ppm. Finally, helium was introduced as a new process gas that allowed to reduce the generation of spatter particles, favouring a stable melt pool, without significantly disrupting the residual stress state of the built part, which is critical for the productivity of L-PBF.

Keywords: Additive manufacturing; Laser powder bed fusion; Process atmosphere; Process stability; Spatter particles; Residual oxygen; Argon; Nitrogen; Helium; 316L stainless steel; Alloy 718; Ti-6Al-4V; AM process productivity; Residual stresses.

PREFACE

The work presented in this doctoral thesis was conducted at the Department of Industrial and Materials Science, Chalmers University of Technology (Gothenburg, Sweden) and the Linde Global Development Centre for Additive Manufacturing (Unterschleissheim, Germany) between October 2016 and December 2020. Linde hosted the candidate for a 18 months research stay. The research has been conducted under the academic supervision of Prof. Eduard Hryha and the industrial supervision of Pierre Forêt. Prof. Lars Nyborg acted as examiner and co-supervisor.

The thesis consists of an introductory part focusing on gas-related aspects for the studied process, followed by a summary of the work performed and summarised in the appended ten papers, as presented below. Four patent applications were generated during this work as well.

- Paper I:** **Effect of argon and nitrogen atmospheres on the properties of stainless steel 316 L parts produced by laser-powder bed fusion**
C. Pauzon, E. Hryha, P. Forêt and L. Nyborg
Materials & Design 179 (2019) 107873
DOI: [10.1016/j.matdes.2019.107873](https://doi.org/10.1016/j.matdes.2019.107873)
- Paper II:** **Oxygen balance during laser powder bed fusion of Alloy 718**
C. Pauzon, A. Raza, E. Hryha and P. Forêt
Materials & Design 201 (2021) 109511
DOI: [10.1016/j.matdes.2021.109511](https://doi.org/10.1016/j.matdes.2021.109511)
- Paper III:** **Effect of residual oxygen in the laser powder bed fusion atmosphere on Alloy 718 spatter oxidation**
A. Raza, C. Pauzon, E. Hryha, A. Markström and P. Forêt
Manuscript
- Paper IV:** **Control of residual oxygen of the process atmosphere during laser-powder bed fusion processing of Ti-6Al-4V**
C. Pauzon, K. Dietrich, P. Forêt, S. Dubiez-Le Goff, E. Hryha and G. Witt
Additive Manufacturing 38 (2021) 101765
DOI: [10.1016/j.addma.2020.101765](https://doi.org/10.1016/j.addma.2020.101765)
- Paper V:** **Mitigating oxygen pick-up during laser powder bed fusion of Ti-6Al-4V by limiting heat accumulation**
C. Pauzon, K. Dietrich, P. Forêt, E. Hryha and G. Witt
Materials Letters 288 (2021) 129365
DOI: [10.1016/j.matlet.2021.129365](https://doi.org/10.1016/j.matlet.2021.129365)
- Paper VI:** **Effect of the process atmosphere composition on Alloy 718 produced by laser powder bed fusion**
C. Pauzon, A. Markström, S. Dubiez-Le Goff and E. Hryha
Manuscript

Paper VII: Argon-helium mixtures as laser-powder bed fusion atmospheres: Towards increased build rate of Ti-6Al-4V

C. Pauzon, P. Forêt, E. Hryha, T. Arunprasad and L. Nyborg

Journal of Materials Processing Technology 279 (2020) 116555

DOI: [10.1016/j.jmatprotec.2019.116555](https://doi.org/10.1016/j.jmatprotec.2019.116555)

Paper VIII: Reduction of incandescent spatter with helium addition to the process gas during laser powder bed fusion of Ti-6Al-4V

C. Pauzon, B. Hoppe, T. Pichler, S. Dubiez-Le Goff, P. Forêt, T. Nguyen and E. Hryha

Manuscript

Paper IX: Residual stresses and porosity in Ti-6Al-4V produced by laser powder bed fusion as a function of process atmosphere and component design

C. Pauzon, T. Mishurova, S. Evsevleev, S. Dubiez- Le Goff, S. Murugesan, G. Bruno and E. Hryha

Manuscript

Paper X: Effect of the process gas and scan speed on the properties and productivity of thin 316L structures produced by laser-powder bed fusion

C. Pauzon, A. Leicht, U. Klement, P. Forêt and E. Hryha

Metallurgical and Materials Transactions A 51 (2020) 5339-5350

DOI: [10.1007/s11661-020-05923-w](https://doi.org/10.1007/s11661-020-05923-w)

Contribution to the appended papers

I, VI, VII: The author planned and performed most of the experimental work. The author analysed the results in collaboration with the co-authors. The author wrote the papers in close cooperation with the co-authors.

II, III: The author planned and conducted the experiments in collaboration with the co-author. The author conducted the SEM analysis, analysed the results, and wrote the papers with the co-authors. The XPS analysis was conducted by A. Raza.

IV, V: The samples were produced at Linde by K. Dietrich. The author planned the study with K. Dietrich and conducted the material characterization. The author wrote the papers in collaboration with the co-authors.

VIII: The author planned most of the experimental work and conducted the experiments on the EOS M290. The shadowgraphy was performed by B. Hoppe and T. Pichler at Fraunhofer ILT. The author analysed the data and wrote the paper in collaboration with the co-authors.

IX: The author planned the experiment. The materials were produced at Linde by S. Dubiez-Le Goff and S. Murugesan. The author conducted the microstructural investigations. The computed tomography and the residual stress measurements were conducted in Berlin by T. Mishurova and her colleagues at the Bundesanstalt für Materialforschung und-prüfung (BAM). The EBSD maps were collected with the support of Y. Yao at Chalmers University of Technology.

X: The author planned and conducted the experiments and analysis in collaboration with A. Leicht who performed the EBSD measurements. The author wrote the paper in collaboration with the co-authors.

Papers not appended to this thesis

- A: **Effect of argon and nitrogen atmospheres on the properties of the as-built 316L stainless steel components by Laser Sintering**
C. Pauzon, E. Hryha, P. Forêt and L. Nyborg
Proceedings of EuroPM2017, Milan, Italy 2017
- B: **Effect of Helium – Argon mixtures as Laser-Powder Bed Fusion processing atmospheres on the properties of the built Ti-6Al-4V parts**
C. Pauzon, P. Forêt, E. Hryha and T. Arunprasad
Proceedings of WorldPM2018, Beijing, China 2018
- C: **Thermally induced porosity within HIPed Ti64 parts: effect of entrapped argon versus Helium in L-PBF**
C. Pauzon, S. Dubiez-Le Goff, P. Forêt and E. Hryha
Proceedings of EuroPM2019, Maastricht, Netherlands 2019
- D: **Effect of part thickness on the microstructure and tensile properties of 316L parts produced by laser powder bed fusion**
A. Leicht, C. Pauzon, M. Rashidi, U. Klement, L. Nyborg and E. Hryha
Accepted in Advances in Industrial and Manufacturing Engineering

Patent applications

1. EP3628419A1 Method and device for feeding gas to an additive manufacturing space
Applicant: LINDE AG, Inventors: T. Arunprasad, C. Pauzon, A. Torres
2. EP3628420A1 Method, gas and device for additive manufacturing
Applicant: LINDE AG, Inventors: D. Bauer, P. Forêt, C. Pauzon, J. Scholz
3. EP3670031A1 Method and system for generating a three-dimensional workpiece
Applicant: LINDE GMBH, Inventors: S. Dubiez Le-Goff, C. Pauzon
4. EP3670030A1 Method and system for generating a three-dimensional workpiece
Applicant: LINDE GMBH, Inventors: P. Forêt, E. Hryha, C. Pauzon, S. Wiberg

CONTENTS

ABBREVIATIONS	viii
CHAPTER 1: INTRODUCTION	1
1.1 Background	1
1.2 Objectives.....	5
1.3 Research scope and approach.....	5
CHAPTER 2: LASER POWDER BED FUSION	7
2.1 Principle	7
2.2 Process parameters	8
2.3 Process stability.....	9
2.4 Residual stresses.....	11
2.5 Process productivity	12
CHAPTER 3: PROCESS ATMOSPHERE	13
3.1 Gases	13
3.2 Establishment of the process atmosphere in the L-PBF chamber.....	13
3.3 Oxygen sensors	14
3.4 Role of the process atmosphere.....	15
CHAPTER 4: 316L STAINLESS STEEL.....	21
4.1 Microstructure development and properties.....	21
4.2 Effect of oxygen and nitrogen.....	22
CHAPTER 5: ALLOY 718.....	25
5.1 Microstructure development and properties.....	25
5.2 Effect of oxygen and nitrogen.....	26
CHAPTER 6: Ti-6Al-4V	27
6.1 Microstructure development and properties.....	27
6.2 Effect of oxygen and nitrogen.....	28
CHAPTER 7: DEFECTS CONNECTED TO THE PROCESS ATMOSPHERE.....	29
CHAPTER 8: EXPERIMENTAL METHODS	31
8.1 Laser powder bed fusion process	31
8.2 Material characterization.....	33
8.2.1. Metallographic preparation	33
8.2.2. Imaging techniques	33
8.2.3. Non-imaging techniques	35

8.3	Process characterization	39
CHAPTER 9: RESULTS AND DISCUSSION	41	
9.1	Residual oxygen in the process atmosphere.....	41
9.2	Gas type.....	46
9.3	Toward process stability and productivity increase	48
CHAPTER 10: CONCLUSIONS	51	
CHAPTER 11: OUTLOOK	55	
ACKNOWLEDGEMENTS.....	57	
REFERENCES	59	

ABBREVIATIONS

AM	Additive Manufacturing
ASTM	American Society for Testing and Materials
BSE	Backscattered Electrons
BCC	Body Centered Cubic
BCT	Body Centered Tetragonal
CAD	Computer Aided Design
DED	Directed Energy Deposition
DIN	Deutsches Institut für Normung
EBM	Electron Beam Melting
EBSM	Electron Backscattered Diffraction
EDD	Energy Dispersive Diffraction
EDS	Energy-Dispersive X-ray Spectroscopy
FCC	Face Centered Cubic
HIP	Hot Isostatic Pressing
HR SEM/SEM	High Resolution – Scanning Electron Microscopy
ISO	International Organization for Standardization
LOM	Light Optical Microscopy
L-PBF	Laser Powder Bed Fusion
NTP	Normal Temperature and Pressure
PDAS	Primary Dendrite Arm Spacing
PDF	Powder Diffraction Files
PM	Powder Metallurgy
PSD	Particle Size Distribution
RQ	Research Question
RS	Residual Stress
SE	Secondary Electrons
SLM	Selective Laser Melting
STL	STereo-Lithography
TIP	Thermally Induced Porosity
UTS	Ultimate Tensile Strength
SXCT/XCT	Synchrotron-based X-ray Computed Tomography
XPS	X-ray Photoelectron Spectroscopy
XRD	X-Ray Diffraction
YS	Yield Strength

CHAPTER 1

INTRODUCTION

1.1 Background

Metal additive manufacturing (AM) covers various processes that allow to build 3D parts by selectively consolidating metal precursors, usually following a layer-wise approach. Among these technologies are powder bed fusion, directed energy deposition (DED) and binder jetting, as listed in the ISO/ASTM F52900 standard¹. These technologies enable, to some extent, the production of complex components with limited material waste in short development times. This grants design optimization, such as for lightweight or customized products. These advantages explain the broad interest and adoption of laser based powder bed fusion by many industrial segments, from aerospace to medical applications². The standard terminology for the process has been defined in recent standard as being laser based powder bed fusion³, although the more broadly adopted wording, laser powder bed fusion and acronym L-PBF, is used in the presented thesis and appended papers.

According to the AMPOWER Report 2020², L-PBF represented the largest share of the metal AM market in 2019 (about 88% with 9111 machines present worldwide), followed by DED (about 6% of the market with 585 installed systems)². Reported in the same summary, more than 5000 tons of powder and wire feedstock were sold by the metal AM market in 2019, with more than 1700 tons of Ti-6Al-4V, 1300 tons of stainless steel and 670 tons of nickel-based alloys². Interestingly, the fastest growing material consumption has been reported for copper and bronze since 2018², which is connected to the interest in complex parts with high thermal and electrical conductivity⁴.

Concrete application examples of L-PBF are numerous and one, which capitalized from the integration of functionalities, is the HYDROPOX® burner used to treat glass surfaces and remove mould-related defects, redesigned by Linde's engineers. The new design replaces 15 parts previously assembled together and includes a complex inner structure with cooling channels to reduce thermal stresses; and is produced in stainless steel in only five hours by L-PBF, see Figure 1. In a similar approach, ArianeGroup used L-PBF of Alloy 718 to produce the next generation of injection heads for rocket engines⁵. The complex assembly of 248 components was replaced by a single element, and production on a multi-laser system cut the production time significantly, from three months, considering the casting route followed by machining, to 35 hours on a four-laser EOS M400-4⁵.

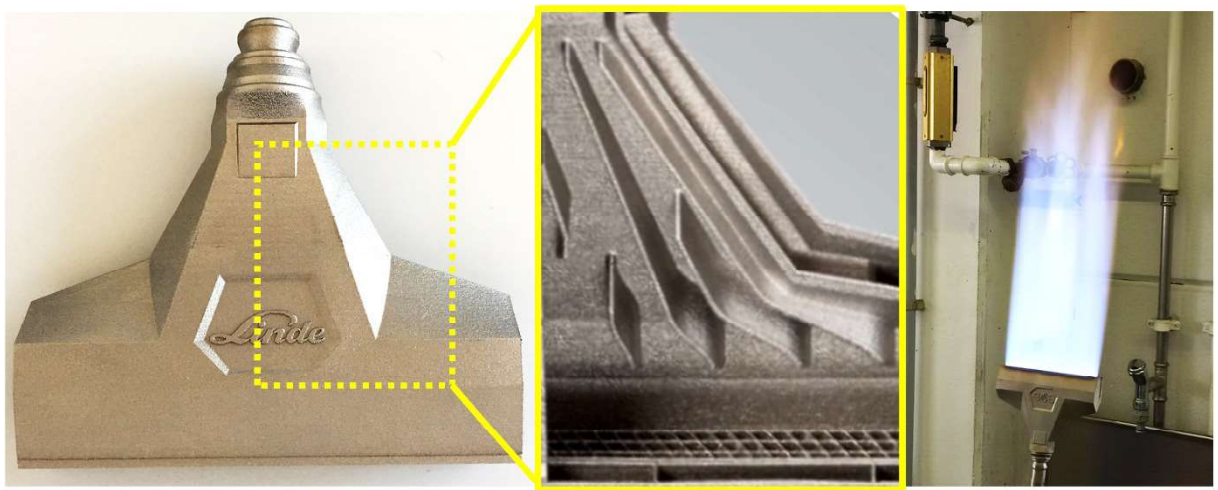


Figure 1: Redesigned Linde HYDROPOX® burner for glass surface treatment produced by L-PBF in steel. The insert depicts the internal structure. The testing of the new design is displayed to the right (Source: Linde GmbH).

Laser powder bed fusion and other AM technologies and concepts have reached different maturity levels. These levels were presented for the first time in 2007 by Gartner Inc. on a hype cycle. In Figure 2, an interpretation of the context in which this thesis was conducted is proposed in a format similar to the hype cycle for 3D printing. This interpretation allows for sorting different concepts under distinct phases, where for example 4D printing is at an early development stage and attracts attention, while bio-printing is getting less attention. Figure 3a and b illustrate these two fields using examples. Other concepts quickly reach the productivity plateau as they answer urgent needs, such as service bureaus supporting companies with the adoption of 3D printing. Certain concepts very rapidly gain a lot of scrutiny such as the printed ventilator valves, door handle openers, or visors mass-produced during the COVID-19 pandemic. These are mostly polymer products fabricated by material extrusion. As Longhitano et al.⁶ explained, these solutions, proposed in record time, have not necessarily undergone clinical testing and validation, nor have they received the ISO 13485 (Medical Devices Quality Management System) certification.

Powder bed fusion was placed in the downward slope of expectations on the hype cycle, depicting a disillusion period as proposed by Gartner Inc.⁷ (as of 2018) and is synonymous with a slight drop in interest. Indeed, metal L-PBF presents several challenges connected to the rapid layer-wise solidification. Regardless of the processed metal, the solidifying layer is exposed to high heating and cooling rates. However, knowledge of phase transformations during such a rapid solidification on the micro-scale based on the existing thermodynamic data is limited, as the solidification speeds overpass that of diffusion, resulting in supersaturated phases. The repeated thermal cycles during printing are also associated with material re-melting and localised diffusion, from which complex and hierarchical microstructures can emerge. The high temperature cycles experienced can also lead to significant segregation and residual thermal stresses, the significance of which depends on the process parameters and processed material. Another general L-PBF aspect is the directional temperature gradient resulting in textured microstructures and an anisotropic mechanical response. Therefore, a considerable amount of work is needed to bridge the remaining knowledge gaps. Thankfully, powder bed fusion is expected to reach the productivity plateau within 5 to 10 years⁷, when it will have proven its economic viability and been adopted by the larger manufacturing community.

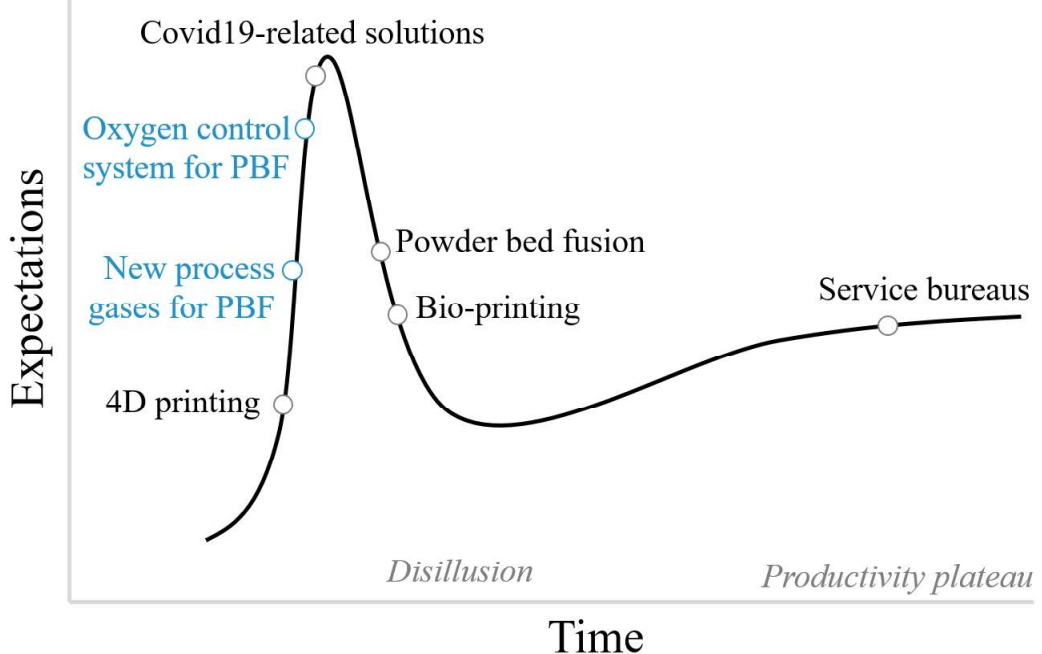


Figure 2: Interpretation of the hype cycle for 3D printing at the time of this thesis disputation, redrawn⁷ with relevance for the work presented herein.

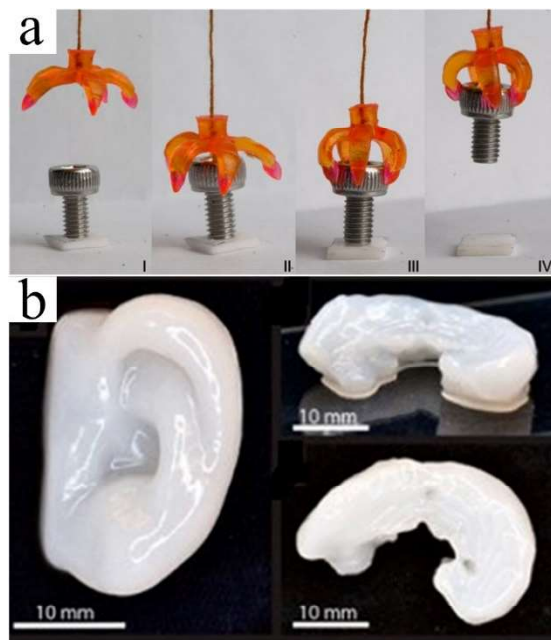


Figure 3: Examples from concepts presented in the hype cycle for 3D printing: (a) 4D printing⁸, and (b) bio-printing reprinted with permission from (*Biomacromolecules* 2015, 16, 5, 1489–1496)⁹ Copyright 2021 American Chemical Society.

Meanwhile, L-PBF continues to soar and conquer new markets, with a growing material portfolio and increasing robustness resulting from collaboration between end-users, machine manufacturers and researchers. A lot of efforts were focused to address the mentioned challenges by comprehending the effect of process parameters on the printed parts and on the process, while simultaneously developing the necessary characterization and monitoring tools. This general success is also highlighted by the impressive increase in AM- and L-PBF-related publications over the last decade, see Figure 4.

The L-PBF atmosphere as a process parameter of its own, has been overlooked in favour of laser and material variables, and mostly considered as a mean to minimize oxidation and remove possible by-products from the laser-powder interaction area. Consequently, the process gas scope has been limited to argon and nitrogen for some alloys, and the guidelines for suitable atmosphere purity have not been formulated. Since the beginning of this thesis work, new process gases for PBF have gained considerable attention. With the first results, expectations for the development of gas and gas mixtures for targeted material and purposes began to grow. In addition, oxygen control for PBF has started to establish itself as an important matter with the development of atmosphere purity control hardware now commercialised¹⁰.

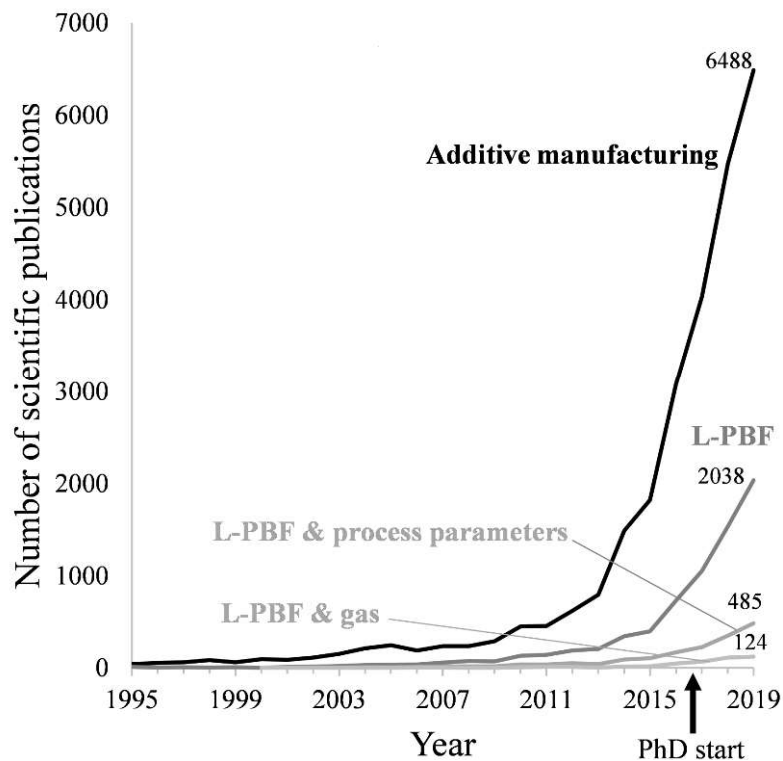


Figure 4: Number of scientific publications per year containing the following topics in their title, abstract, or keywords: Additive manufacturing, L-PBF, L-PBF and process parameters, and L-PBF and gas. L-PBF includes both the acronym L-PBF and the trademark SLM. The data were collected using the online database Scopus.

1.2 Objectives

The aim of the study presented in this thesis was to investigate how the process atmosphere influences the properties of L-PBF-produced material and the stability and productivity of the L-PBF process. The objectives are summarized in the following research questions (RQ):

RQ 1: How does the purity of the L-PBF process atmosphere influence the process stability and material properties?

RQ 2: How does the type of L-PBF process atmosphere influence the material properties?

RQ 3: How does the type of L-PBF process atmosphere influence the process stability and productivity?

These research questions were addressed considering the alloys most commonly used by the AM community: 316L stainless steel, Alloy 718 and Ti-6Al-4V².

1.3 Research scope and approach

The scope of the thesis is summarized in Table 1. A variety of materials and gas types were investigated, and the methodology was adapted to the studied materials to address the research questions. The characterization involved both the study of the powder and the built materials, as well as in situ investigations of the L-PBF process.

The study of the atmosphere purity (RQ 1) was initiated by establishing the status of state-of-the-art hardware at the time (i.e., gas supplies and control solutions) and their effect on the properties of built 316L stainless steel (Paper I). This work highlighted the non-negligible influence of environmental impurities on powder degradation by the selective oxidation of Cr, Mn and Si. The work connected to RQ 1 therefore included Alloy 718, which is sensitive to the exposure to impurities because of its alloy composition containing, in addition to Cr, elements with higher affinity to oxygen, such as Al and Ti. To understand the atmosphere purity effect during L-PBF processing, a general oxygen balance of the L-PBF process was investigated to determine the mechanism and extent of the impurities picked-up by Alloy 718 (Paper II). This showed that spatters gain most of their oxygen from the process atmosphere, resulting in coverage of their surface by oxide features. Therefore, the possibility to mitigate the oxidation of the Alloy 718 spatter by reducing the residual oxygen in the process atmosphere was shown (Paper III). Finally, the third material studied, Ti-6Al-4V, is undoubtedly the most vulnerable to oxygen and nitrogen exposure under L-PBF conditions. The focus was on both, the effect of the oxygen control during L-PBF (Paper IV) and the effect of heat accumulation (Paper V), on the oxygen and nitrogen pick-up and the resulting properties of Ti-6Al-4V specimens.

In parallel to RQ 1, the effect of nitrogen as a L-PBF process gas compared to argon (RQ 2) on the properties of 316L stainless steel and Alloy 718 was further addressed in Papers I, VI and X.

RQ 3, which is connected to the study of a new range of process gases toward increasing process stability and productivity, was mostly considered for Ti-6Al-4V (Papers VII-IX).

As the results revealed a significant potential for productivity increase, the use of helium and its mixes was further evaluated for 316L stainless steel (Paper X). The initial work led to collaborations with Fraunhofer ILT to conduct in situ shadowgraphy (Paper VIII) and with the Bundesanstalt für Materialforschung und-prüfung (BAM) to perform residual stress measurements (Paper IX).

Table 1: Research questions addressed in the appended papers. The colours identify the materials studied: blue for 316L stainless steel, orange for Alloy 718, and green for Ti-6Al-4V.

	RQ 1	RQ 2	RQ3	Material	Gas
Paper I				316L stainless steel	Argon, nitrogen
Paper II				Alloy 718	Argon
Paper III				Alloy 718	Argon
Paper IV				Ti-6Al-4V	Argon
Paper V				Ti-6Al-4V	Argon
Paper VI				Alloy 718	Argon, nitrogen
Paper VII				Ti-6Al-4V	Argon, helium
Paper VIII				Ti-6Al-4V	Argon, helium
Paper IX				Ti-6Al-4V	Argon, helium
Paper X				316L stainless steel	Argon, helium, nitrogen

CHAPTER 2

LASER POWDER BED FUSION

2.1 Principle

Laser powder bed fusion uses the heat generated from a laser to selectively melt areas of a powder bed in a layer-wise manner to produce components. As simple as this process seems, it requires some time for preparation and manual work before and after the machine has completed its tasks. The production sequence starts with the definition of the component's design, which can be generated using computer-aided design (CAD) software. The data created as such is often a CAD file containing 2D and 3D graphics and possibly other details, such as material and dimensions. From this CAD file, a STL (stereo-lithography) file, which is a triangular representation of the surface geometry of the design, is generated. This STL file is the usual input data for the dedicated AM software responsible for preparing the information transferred to the AM machine. In short, the AM software allows to place and orient the design within the virtual build volume, define support structures, material and process parameters, and produce the file holding this information in a readable format for the AM machine. The actual transfer of this file is completed either by placing the data on a drive, which is physically connected to the AM machine, or via an online connection.

In addition to this data preparation, the L-PBF machine needs to be prepared by loading it with the feedstock powder and the baseplate on which the component is built and conducting routine procedures, such as checking the optics and sealings. When exposed to the metallic powder particles, the operator has to wear personal protective equipment, such as a suit, gloves, filter mask, goggles and anti-static shoes. The size of L-PBF systems, and thus the ease with which they can be handled, varies significantly to address many applications, from process development on a laboratory scale with volumes of a few cm³ to large industrial volumes close to 1 m³. Most L-PBF systems have the following elements in common within their process chambers, as illustrated in Figure 5: an optical system including the laser and the scanning solutions, a building platform on which a baseplate is set to support the printed components, a powder dispensing system with a container and a recoater, as well as a collector for the excess powder. The printing sequence usually includes spreading an even powder layer on the baseplate, the laser scans the powder bed according to the components' design, followed by the lowering of the baseplate by the building platform. Then, the application of a subsequent even layer of powder on the previous one is followed again by the laser scanning. This process is repeated until all the components placed in the virtual build volume have been produced to their full height.

When the L-PBF process is finished, the building platform is lowered by the height of the produced components, which are surrounded by un-melted powder. Therefore, the operator has

to remove the non-used powder, raise the platform, and remove the baseplate. At that time, other routine actions, such as sieving the used powder and reloading the machine, can also be performed. The withdrawn baseplate may then go through different post-AM treatments until the components are removed. Thereafter, the obtained components may require additional support removal and undergo surface treatment.

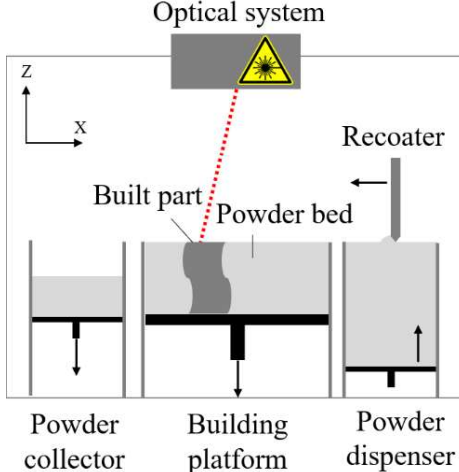


Figure 5: Schematic of the L-PBF process chamber seen from the side.

2.2 Process parameters

The properties of components produced by L-PBF depend on the routine followed along the process chain: from the preparation of the machine to post-processing with, e.g. heat treatments and machining operations, through the printing itself. Some steps may be more critical for certain alloys, such as different post-AM treatment, as well as powder storage and re-use have to be considered. The process parameters and, in particular, the laser-related parameters (such as laser power, scanning speed, hatch distance, etc.) are the most relevant when it comes to the density and thus the quality of the material in its as-built state.

The scanning speed defines the rate at which the laser travels on the build area and is typically limited to 7000 mm/s. The scan vector indicates the direction of the laser's movement. The hatch distance is the distance between two scan vectors. Finally, the laser power and the layer thickness are also key parameters. The melt pool forms when the laser beam of an approximate spot size of 100 µm heats up by radiating the powder bed target above its melting point. The presence of the powder particles promotes the laser absorption by multiple reflections and scattering on their surfaces¹¹. As the melt pool's travel follows the laser spot, it tends to exhibit a teardrop shape as sometimes observed in welding. To ensure a high as-built density, the parameters are tuned so that the radiation re-melts three to five already deposited layers, and the scan vectors overlap sufficiently.

Many other process variables have been identified, and include the build plate temperature, the recoater speed, and the most complex one, the scan strategy. The machine manufacturers usually offer complete parameter sets dedicated to specific materials. However, despite the many recognized advantages of L-PBF, its adoption by the greater number of users is limited by the AM community's relatively limited understanding of the physical phenomena involved during the process. Numerous efforts are currently focused on studies of laser-related parameters' interactions and effect on the microstructure formation.

2.3 Process stability

Melt pool flow

The melt pool flow, or the movement of the liquid melt, is closely connected to its temperature and chemistry. The temperature within the melt pool describes a gradient with the highest temperature at the centre of the laser spot. This gradient causes variations in surface tension, which usually decrease with increasing temperature. Typically, the centre of the melt pool with lower surface tension tends to flow outward to the edges of higher surface tension. This is the Marangoni flow, see Figure 6a. The presence of surface-active elements, such as sulphur, may reverse the Marangoni flow^{12,13}. In addition, as the metal density decreases with higher temperatures, buoyancy also drives the melt outwards, i.e. the hot liquid in the centre floats, while the cooler liquid sinks along the melt pool boundaries toward its bottom.

At the centre of the laser spot, the temperature is well above the melting point of the material processed. As for other laser processes connected with metal heating up to fusion, metal vapours are formed above the melt pool surface¹⁴. The extent of vaporization can be reduced upon higher pressures. High-speed imaging of the L-PBF process has shown that metal vapours expand vertically against the ambient gas and the gas flow. This expansion applies a pressure, called the recoil pressure on the melt pool surface. This pressure tends to drive the melt down- and outward from the laser spot, see Figure 6b. For high enough recoil pressure, a depression forms, i.e. the keyhole. In addition to the possible generation of a keyhole, the rapid expansion of the vapours can create a lateral gas flow close to the melt pool, directed toward the vapour expansion¹⁵. This flow can pull particles toward the melt pool and upward, resulting in a denudation zone around the scanned area, deprived of particles. These pulled particles are referred in the literature as entrained particles. Bidare et al.¹⁶ estimated the vapour ejection velocity to be about 100 m/s for 316L stainless steel, approximately 2 mm above the build plate for a 200 W laser power and decelerating exponentially in the z direction.

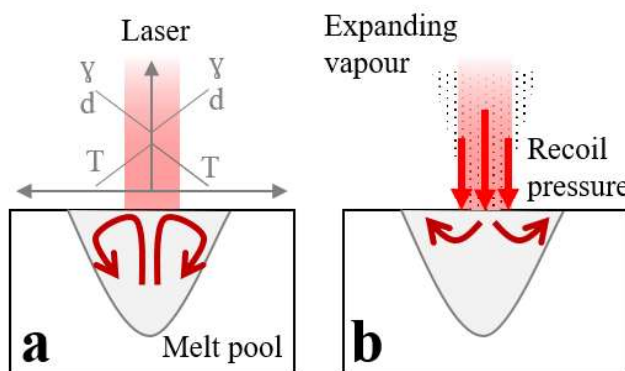


Figure 6: Schematic representation of the convection flow inside the melt pool connected to (a) the Marangoni flow and buoyancy, and (b) the recoil pressure.

Spatter generation

The rapid local heating of the powder bed results in the quick expansion of the gas in the interparticle spaces, which can result in their expulsion. These accelerated metal particles can be taken in the protective laminar gas flow and/or fall on the powder bed, intersect with the moving laser, or add to the melt pool. The melt pool flow is also responsible for the generation of spatter. If the convection forces in the melt overcome the surface tension, direct ejections

from the melt pool are generated. These ejections are characterized by completely different thermal histories than those of the virgin powder particles in the powder bed, typically produced by gas atomization.

Spatters were divided between hot and cold particles by Ly et al.¹⁷ Cold particles comprise entrained particles, which may have experienced surface heating observed as oxidation and/or recrystallisation, while hot particles underwent partial to full re-melting observed as changes in surface appearance, composition, or microstructure. The authors distinguish these particles from “recoil pressure induced ejections”, which are direct melt pool ejections. Under the processing conditions tested, Ly et al.¹⁷ estimated that recoil pressure-induced ejections have velocities in the range of 3 to 8 m/s and account for 15% of the total generated spatter. Cold particles account for 25% of the spatters with velocities between 2 to 4 m/s, and hot particles account for 60% with velocities between 6 to 20 m/s.

Complex agglomerates are also likely to form from the collision of melt and metal particles. Hot particles, both entrained and direct melt pool ejections, and vapour fumes are especially undesirable as they cause laser shadowing by absorption of the radiation, and scattering, that leads to laser defocusing and reduced transferred energy to the material. In general, spatters experience high temperatures, which trigger the mass transfer of elements of high affinity to oxygen from the volume to the surface of the particles. These spatters are likely to be conserved through the process chain as they are not necessarily removed during the sieving operation. This conservation of spatter particles can lead to the transfer of oxygen and oxide inclusions to the as-built material, resulting in the formation of inclusions and in more severe cases lack-of-fusion porosity. Figure 7 illustrates the phenomena involved in spatter generation described in this section.

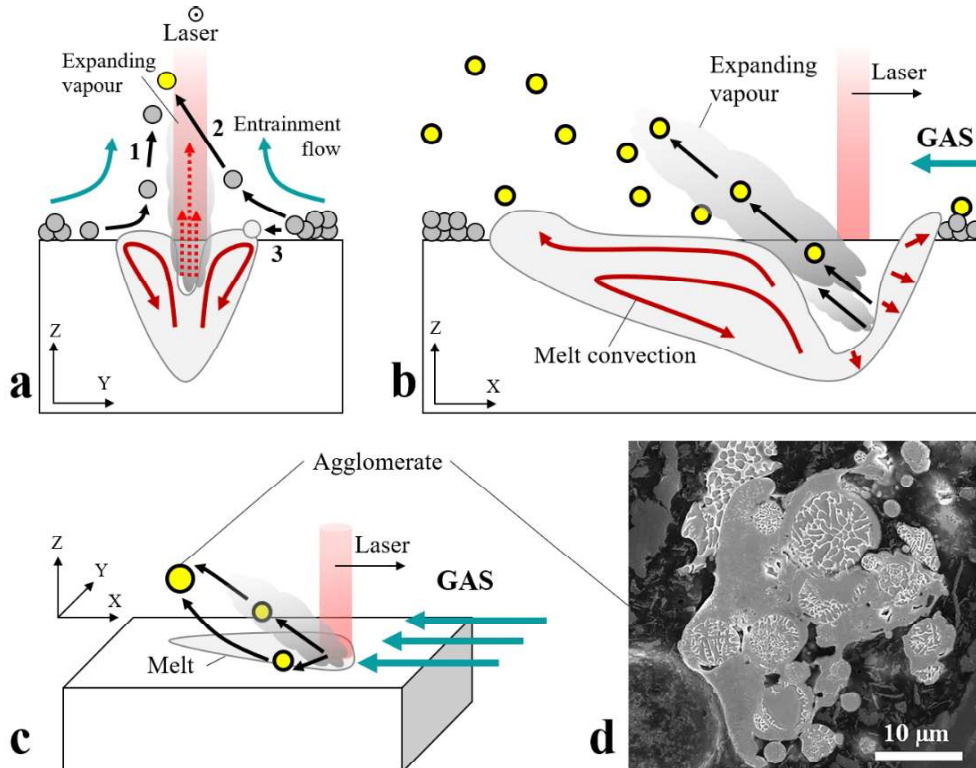


Figure 7: Schematics of spatter generation during L-PBF. (a) Generation of entrainment-induced spatters; (b) Expanding vapour perpendicular to the front wall of the keyhole, with generation of spatters backwards; (c) backward generation of spatters and possible agglomeration by collision between hot and cold spatters; (d) SEM micrograph of a Alloy 718 spatter cross-section highlighting the agglomeration of spatters and/or melt ejecta.

L-PBF monitoring

As introduced, the L-PBF process is connected to relatively complex, multiple and not yet fully-understood physical phenomena. Process monitoring tools are recently developed to increase the current understanding and identify the events relevant to the process stability. Laboratory-scale L-PBF systems have been designed for *in situ* monitoring by imaging of the melt pool¹⁸, imaging of the larger interaction area of the laser with the melt pool to capture spatter generation¹⁹, or diffraction techniques to track the phase transformation of the processed metal²⁰. The development of such tools to follow this highly dynamic process has been strongly supported by the faster detectors and cameras available today. Larger industrial systems are now also integrating monitoring devices, allowing for example to detect variations in emitted intensity by the melt pool at the scale of the baseplate²¹. Identifying the signatures of defects in this considerable amount of collected data appears to be a challenging task but will allow the close-loop control, to adjust the laser parameters for improved material quality and reproducibility.

2.4 Residual stresses

The residual stresses obtained from L-PBF can compromise the integrity of the built components. These stresses arise from the complex thermal history experienced by the material during processing. According to Mercelis and Kruth²², the stresses are caused both by the temperature gradient around the laser spot and the cool-down of the molten top layers, which explains the strong influence of laser parameters. These stresses build up at a micro-scale for each layer and result in the development of residual stresses at the component's level, sometimes referred to as type I²³. These macroscopic stresses arise from non-uniform plastic deformation within the built part. The residual stresses in the component in static equilibrium (free from external forces) are limited by the elastic limit of the produced material²⁴. Tensile residual stresses are the most undesirable, as they can, for example, enhance cracking and thus limit fatigue properties.

Mishurova et al.²⁵ demonstrated that the tensile residual subsurface stresses along the building direction in Ti-6Al-4V decrease with increasing laser energy input. This result was attributed to the laser's larger affected volume and thus the reduced thermal gradient. These large subsurface tensile stresses are balanced by bulk compressive stresses²⁶. In addition, during printing the part's distortions are limited by the baseplate. Thus, it is not uncommon to observe the deformation of a component as it is removed from the baseplate because of the redistribution of stresses to ensure equilibrium of the new geometry. To avoid these deformations and not compromise geometric tolerances, stress relief heat treatments can be applied after L-PBF, while the component is still on the baseplate.

Large local stresses exceeding the yield limit can lead to plastic deformation of the part during the process and a premature build job failure as the recoater is blocked by the warped component top surface, sometimes referred to as curling. In addition to optimized laser parameters and baseplate pre-heating, the support structures are also preventing component's distortions; however, their removal can be time consuming and limit the overall process productivity.

2.5 Process productivity

Productivity is usually understood as a measure of the output per unit of input²⁷ or as the efficiency to transform input into useful output²⁸. For L-PBF, productivity is connected to achieving the production of parts at a minimum cost and not at the expense of quality, e.g. density, defect distribution, residual stresses and mechanical properties. Improving the productivity is one of the main challenges to make L-PBF more economically feasible and address a broader range of applications. Several strategies can be followed in that pursuit. Among these strategies, the build rate, defined as the product of the laser scanning speed, the hatch distance and the layer thickness, can be increased. The utilisation of the build volume can be enhanced to produce more parts on a single baseplate and reduce the time spent on machine preparation. This can be achieved by adapting the part design, placement and orientation. The optimization of the AM design to reduce the necessary melted volume by integrating complex features, hollow sections, and lattice structures is also a solution to decrease the build time. In addition, efforts are focused on improving the hardware capabilities with the development of high power²⁹ and multi-laser systems³⁰, the build volume increase³¹, hybrid system development³² and process automation³³. The growth of machine and material portfolios and the increase in competitiveness between the manufacturers also support the decrease of material and hardware costs. Finally, the definition of standards³⁴ and the education of technicians and engineers in this new manufacturing field will drive the development and innovation in the field of AM³⁵.

CHAPTER 3

PROCESS ATMOSPHERE

3.1 Gases

Laser powder bed fusion systems are usually connected to an external gas supply, which can be single steel cylinders with a volume capacity of 50 L and a filling pressure of 200 bars, cylinder bundles with 12 cylinders, or large cryogenic tanks storing liquids that are later vaporised for use, depending on the users' needs. A few machines, such as the EOS M290, also offer economical built-in gas supply options, such as a nitrogen generator. This system produces nitrogen from compressed ambient air, initially rich in nitrogen, by filtering it, e.g. with adsorptive material that specifically traps some gas species. While cost-effective, the purities achieved are generally not competitive with that of industrially produced gases. Being scarcer at about 0.9% in ambient air, argon must be produced by fractional distillation of liquid air which achieves high purity, typically 10 ppm impurities. Helium is only present in quantities of about 1 ppm in the air. This gas is therefore produced by the fractional distillation of natural gas, containing up to 4% helium in volume³⁶.

The gas consumption during L-PBF is determined by the volume of the process chamber, the chamber's tightness and the purging strategy followed. On the EOS M290 used in this work, the gas consumption is maximum during the process chamber purging of about 40 L/min for approximately 20 min, while during the printing a holding flow of a few L/min ensures that no impurities enter. These numbers may vary for different systems, depending on technical solution and machine size as well as for example the state of the sealings. Argon is the traditional gas supply option for L-PBF processing.

3.2 Establishment of the process atmosphere in the L-PBF chamber

The external gas supply is commonly connected to the L-PBF system through quick connectors. Series of pressure valves managed by the machine's control system connect the fresh gas to the recirculation system. The recirculation system is a closed gas loop passing through the build chamber, a series of coarse-to-fine filters and a pump that pushes gas back to the chamber through connectors. A homogeneous flow above the build area is desirable and is established by the design of the gas inlet and outlet. Usually, the process atmosphere is generated by a purging sequence during which the gas flow from the external supply to the recirculation system is elevated. When the oxygen level displayed by sensors placed in the system is below a certain value, defined by the settings in the machine, the pump activates the recirculation of the gas in the system. Typically the gas flow from the external supply to the system is finally shut or reduced to a holding flow, which counteracts possible leaks. In general

the build job starts when the system is closed and process gas parameters are stable, when factors like the pump voltage, the oxygen level and the baseplate temperature do not vary significantly. There are some alternatives to this purging method to produce the process atmosphere, such as an alternation between vacuum pumping the air from the process chamber and back-filling with inert gas. However, this solution has still not been broadly adopted by equipment manufacturers. Figure 8 presents a schematic example of gas recirculation in a L-PBF system.

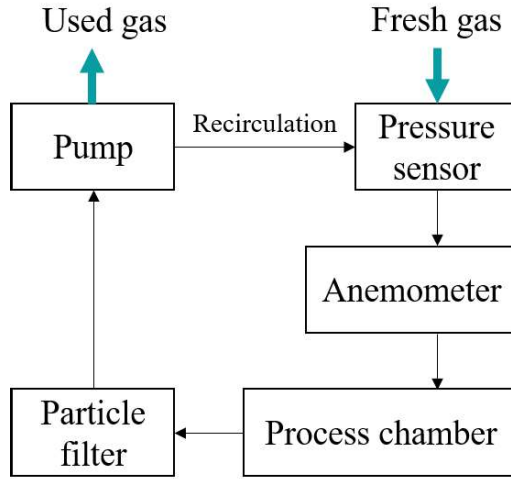


Figure 8: Schematic example of gas recirculation within a L-PBF machine.

3.3 Oxygen sensors

In addition to the design of the hardware and its oxygen control system, the oxygen sensor type can have a significant influence on the purity of the atmosphere achieved. In this section, two types of oxygen sensors typically implemented in L-PBF systems are discussed: the lambda probe and the electrochemical cell.

The lambda probe consists of a doped solid ceramic electrolyte, typically yttrium stabilized zirconia, and two sintered platinum electrodes on both of its sides, which are gas-tight from one another. The probe operates at high temperatures, i.e. 700-800 °C, to allow the transport of oxygen ions through the solid electrolyte. One platinum electrode is on the process atmosphere side, while the other is on the reference side for which $P_{O_2} = 0.21$ bar. The oxygen from the process chamber is reduced at the cathode, travels through the ceramic, and is oxidized at the anode. In the sensor, a current is generated proportional to the rate at which oxygen ions reach the cathode. The electron flow (current) is reversed if the sample's oxygen level exceeds that of the reference, which is unlikely for the current L-PBF systems and gas portfolio. One of the drawbacks of using this high temperature sensor is the enhanced oxidation of species like hydrogen and hydrocarbons at the cathode, which lowers the detected oxygen level and limits the use of this sensor for trace oxygen analysis. However, at operating temperature, the sensor's short response time makes it appropriate to monitor rapid changes.

An electrochemical cell consists of a cathode, an electrolyte and a lead anode. The oxygen from the process chamber enters the cells through a capillary and gets in contact with the cathode, where it is reduced into hydroxyl ions. These ions migrate through the electrolyte toward the lead anode, where they are oxidised and form lead oxide. This generates a current proportional

to the oxygen concentration following Nernst's equation. Ultimately the lifetime of the cell is limited by the amount of lead available and the rate at which it is oxidised, but can be extended by flushing it with low oxygen gas when in stand-by. In addition, excessively dry environments can also be detrimental to the water-based electrolyte's integrity. The sensor is usually calibrated with a reference or calibration gas of an accurately known composition measured using e.g. gas chromatography.

3.4 Role of the process atmosphere

This section presents the current understanding of the L-PBF process gas role and introduces the recent advancements within this field. The primary role of the process atmosphere is to ensure a low residual oxygen level and to remove metal vapours and spatter from the build area. Although seldom mentioned in the literature, the process atmosphere also takes part, to some extent, in the heat transfer during L-PBF.

Residual oxygen

A low residual oxygen level is necessary to hinder the oxidation reactions triggered by high local temperatures at and close to the laser spot and solidified component. The purging of the process chamber allows for the significant dilution of oxygen (about 21% in air) and other impurities, and a typical oxygen threshold value enabling the process initiation is 1000 ppm (0.1%). As Figure 9 illustrates, this value is high since most of the oxides are thermodynamically stable at this oxygen partial pressure, even up to high temperatures. However, the figure applies to pure metal-oxide systems under thermodynamical equilibrium, and considering the far-from-equilibrium nature of L-PBF connected to the high heating and cooling rates, it provides only an indication of oxidation risk and sequence.

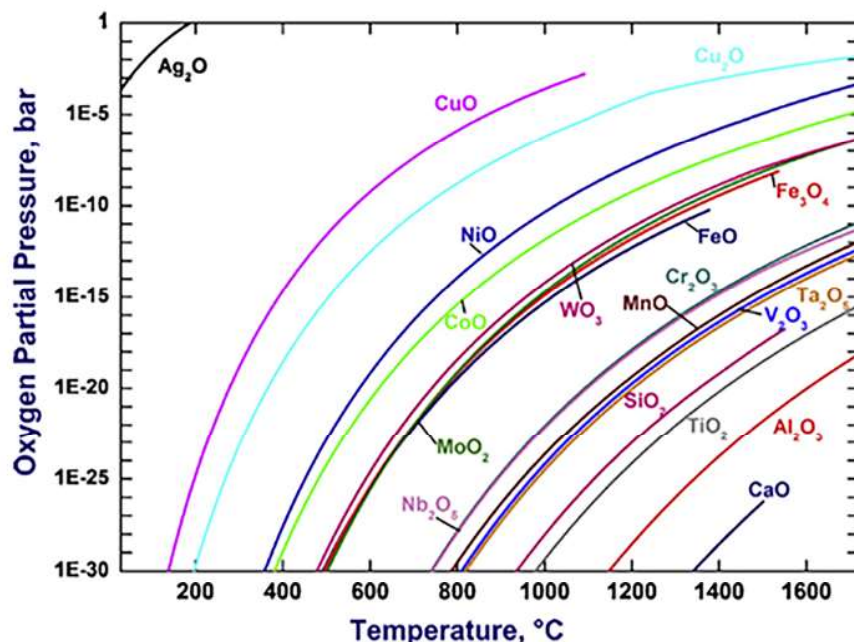


Figure 9: Equilibrium partial pressure of oxygen for some oxide/metal systems (plotted with HSC Chemistry)³⁷.

When the impurity level was on the level of several percent at the early stages of L-PBF technology establishment, the relationship between residual oxygen and balling, which is the formation of discontinuous melt tracks with droplets, was established^{38,39}. It was shown that the formation of oxide on the surface hindered the melt wetting on the previously deposited layers. More recent work has highlighted that oxidation and oxygen pick-up is more critical for Ti-based alloys during L-PBF⁴⁰ than for Fe-based ones⁴¹, which form less-stable oxides and have a lower oxygen solubility limit.

Spatter removal

As mentioned above, the interaction between the laser and the powder bed is associated with metal vaporization, condensate and spatter formation. These results are undesirable as they may reduce the transferred energy from the laser to the metal target. They can also lead to a significant loss of low boiling point species in the as-built material. Generation of defects by spatter, if its trajectory ends on the powder bed, has to be taken into account as well. The gas flow entrains these particles by applying a drag force directed toward the gas outlet. This force is a function of the gas density, the particle area and the gas speed. The gas speed and density should be high enough to displace the vapours and spatter without disrupting the powder bed. Reijonen et al.⁴² found that the spatter and the vapours rise more normally to the melt pool when the argon flow velocities are reduced. They established that a flow of 2 m/s using argon on a SLM125hl (SLM Solutions GmbH) is the minimum velocity necessary to produce quality parts porosity-wise.

Ferrar et al.⁴³ revealed that gas flow uniformity over the build area is essential to achieve high as-built density independent from the part's position. In addition, Schniedenharn and Schleifenbaum⁴⁴ found evidence that spatter particles emitted at the melt pool have high kinetic energies and hence are not directly deviated from their emission direction. Thus, they proposed that it is beneficial to achieve the maximum gas speed, not directly but slightly above the melt pool⁴⁴. Their results highlight that a “b-shaped” gas flow profile, with a non-uniform speed distribution above the process area and a maximum close to the baseplate, is preferred to achieve high material densities compared to a “D-shaped” profile, with a more homogeneous distribution. This argument is also supported by the high ejection velocity of the vapours¹⁶, which are thus dragged by the gas flow only well above the melt pool, see Figure 10.

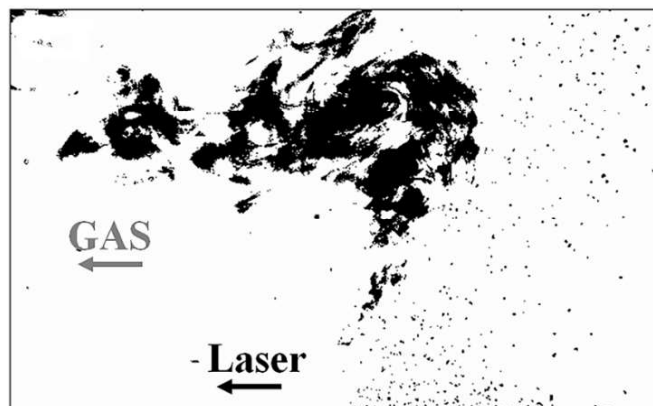


Figure 10: Filtered shadowgraph using ImageJ from single track experiment performed on an AconityMINI at Fraunhofer ILT. The small dark particles are entrained cold particles, and the metal vapour formed above the laser spot appears with dark contrast and is entrained to the left by the process gas (here argon).

Furthermore, research conducted by Chen⁴⁵ indicates that the gas flow sorts the powder and spatter particles by size, and for a medium size L-PBF machines such as the EOS M290 (EOS GmbH), the larger particles ($> 80 \mu\text{m}$ for Ti-6Al-4V) remain on the powder bed. This study further investigated the influence of the part's orientation and laser scan direction with respect to the gas flow and connected it to the surface properties of the built components. As reported by Anwar and Pham⁴⁶, the laser scanning in the same direction as the gas flow should be avoided, e.g. see Figure 10 and Figure 11a, as the spatter tends to be carried in the direction of the laser movement and thus interacts with it. In addition, the results highlighted that the roughness can be mitigated by adjusting the laser exposure order of an individual part on a single build job in the direction against the gas flow. The laser scanning direction and scanning sequence effects are summarized in Figure 11. This detailed study underlined that some positions on the baseplate could suffer from turbulent gas flow, typically close to the gas inlet, outlet and baseplate edges, where the baseplate is slightly offset with the gas inlet and outlet.

Notably, the ability of the gas to remove particles and spatters is dependent on the considered hardware, and more precisely on the design and capabilities of the recirculation system, inlet and outlet design, chamber size, and so on. Systems with large baseplates and multiple lasers have been developed as a solution to the demand for productivity increases, where such an interaction between the scanning sequence and direction becomes significantly more complex.

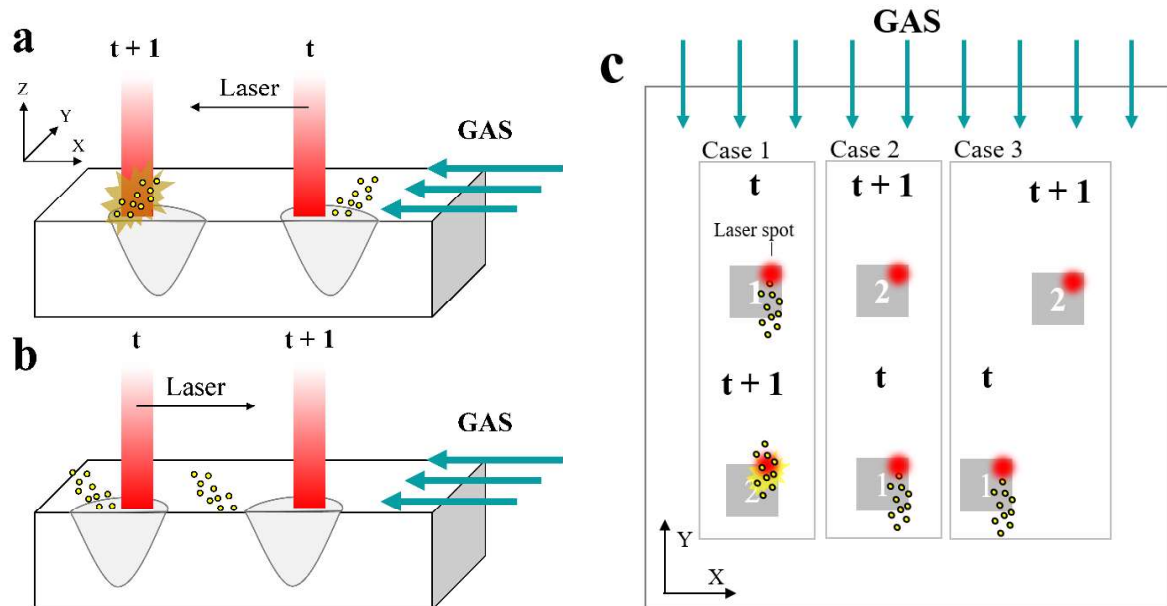


Figure 11: (a, b) Schematic highlighting the dragging of spatter within the laser path when the laser scanning direction is the same as the gas flow, redrawn from Anwar et al.⁴⁶; (c) schematic of the top view of the baseplate displaying the scanning of squared areas in different sequences. This view highlights that scanning first areas close to the gas inlet can lead to the interaction of the produced spatter with the laser when scanning areas further away (Case 1), so the reverse is preferred (Case 2). Placing components so the scanned areas do not align perfectly with respect to the gas flow is recommended (Case 3).

Heat transfer

Some fraction of the laser energy is absorbed by the powder bed. The extent of this absorption depends on the absorptivity of the targeted powder feedstock, which itself varies with factors such as temperature and physical state. The absorbed energy leads to melting the powder bed as long as the latent heat of fusion is overcome. The remaining energy contributes to heating the liquid and the surrounding material as well as vaporization. Heat losses and cooling are induced by conduction through the deposited material and the baseplate, and to a lesser extent to the surrounding powder bed, radiation of the hot material and convection by the process gas. When the gas flows over the melt pool and the solidified layer, heat transfer occurs partly by fluid convection. This convection sweeps away the heat further down the gas stream. For L-PBF, this is forced convection since the gas flow is established by a pump. Heat transfer problems are usually addressed by derivation of the heat transfer coefficient h with unit $\text{W}/(\text{m}^2\text{K})$.

The thermal diffusivity α is also an important property that connects thermal conductivity to the volumetric heat capacity⁴⁷, see Table 2. A gas with a large thermal diffusivity tends to respond quickly to thermal changes. Figure 12 displays the variation of thermal diffusivities of argon and helium as well as their ratio, which is greater than 8 in the temperature range displayed, highlighting the potential for using helium for enhanced thermal diffusion.

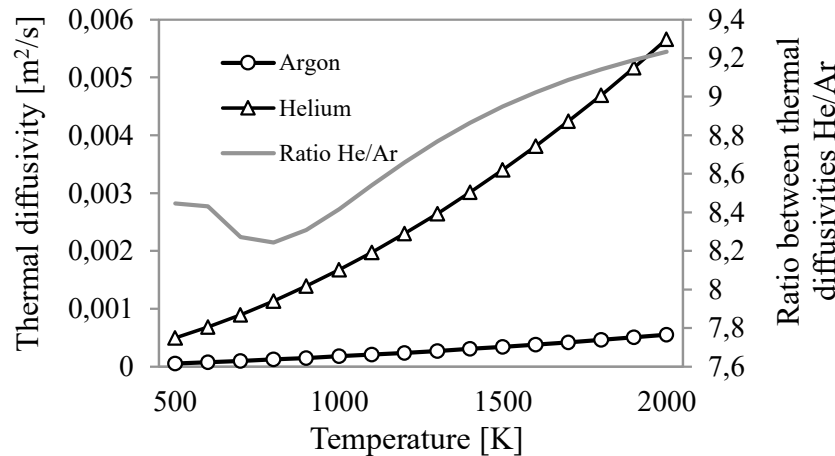


Figure 12: Thermal diffusivities of argon and helium (left y-axis) and their ratio (right y-axis) as a function of temperature.

To understand the relative effect that argon and helium have on the heat transfer, the aspects connected to gas convection can be studied separately. However, it should be stressed that this simplification does not account for the actual complex heat transfers occurring during L-PBF, and that most of the heat transfer occurs through conduction in the solid material.

There are numerous solved simplified heat and mass transfer problems in the literature dealing with forced convection, such as that of a flat plate in a parallel fluid flow or a flow over a sphere. For L-PBF, one can consider the last deposited layer to be a flat plate. Taking into account a gas speed of 2 m/s, a plate length of 5 mm, and a gas temperature of 300 K, the flow over the plate is assumed to be laminar. Under the same conditions, the Prandtl number is 0.66 for both gases. Therefore, assuming that the plate surface is isothermal (strong simplification

because of the important thermal gradient in L-PBF), the following relationship linking the average Nusselt number \overline{N}_u and the heat transfer coefficient \bar{h} ⁴⁷ can be used:

$$\overline{N}_u = \frac{\bar{h}L}{\kappa} = 0.664 Re^{1/2} Pr^{1/3} \quad (Pr \geq 0.6)$$

The ratio $\overline{h_{He}}/\overline{h_{Ar}}$ is approximately 3, highlighting the benefit of using helium to enhance the cooling of the hot deposited layer over argon.

Similarly, for a metal particle with the diameter of 40 μm and initial temperature of 2000 K, travelling at a speed of 10 m/s, one can derive \overline{N}_u and \bar{h} using the correlation of Ranz and Marshall⁴⁷ (free falling liquid droplet), with the gas properties calculated at the average of the particle surface and gas temperatures (1150 K):

$$\overline{N}_u = \frac{\bar{h}L}{\kappa} = 2 + 0.6 Re^{1/2} Pr^{1/3} \quad (Re < 200)$$

At 1150 K, the Reynolds numbers of argon and helium are 2.77 and 0.33, respectively, and the Prandtl numbers for argon and helium are still about 0.66. Therefore, the ratio $\overline{h_{He}}/\overline{h_{Ar}}$ is approximately 7. In addition, for a flying metal particle such as a spatter, the assumption that the problem is a forced convection mode is more accurate than for the last deposited layer.

Table 2: Relevant quantities needed to address the heat transfer problem⁴⁷.

Quantity	Definition	Interpretation
Thermal diffusivity	$\alpha = \frac{\kappa}{\rho C_p}$ With κ as the thermal conductivity, ρ as the gas density, and C_p as the isobaric heat capacity	Ability of the substance to conduct heat relative to its ability to store energy (unit: m ² /s)
Reynolds number (Re)	$\frac{VL}{\nu}$ With V as the gas velocity, ν as the kinematic viscosity, and L as the characteristic dimension	Ratio of the inertia and viscous forces (dimensionless)
Nusselt number (Nu)	$\frac{hL}{\kappa}$ With h as the heat transfer coefficient	Ratio of convection to pure conduction heat transfer (dimensionless)
Prandtl number (Pr)	$\frac{C_p \mu}{\kappa} = \frac{\nu}{\alpha}$ With C_p as the isobaric heat capacity	Ratio of the momentum and thermal diffusivities (dimensionless)

Recent progress

Dai and Gu⁴⁸ modelled the L-PBF process and the resulting top surface morphology of a TiC/AlSi10Mg composite using argon, nitrogen and helium. Their findings suggest that argon favours the stabilization of the melt pool under the formation of a keyhole, compared with the other two gases. Although these results are in contrast with more recent studies, they do indicate that the use of helium affects the generated vapours. Wang et al.⁴⁹ studied the properties of Al-12Si parts produced on a RealizerSLM100 machine using argon, nitrogen and helium. They reported relatively constant densities regardless of the process gas, which can be considered low (about 97%) in comparison to the capabilities of current systems. The authors successfully implemented helium.

Later, Bidare et al.¹⁵ compared the use of argon with that of helium using high-speed and schlieren imaging on a laboratory-scale system for pressures up to 5 bar for 316L stainless steel. They proved that helium was responsible for the lower temperature of the observed vapours which they refer to as “laser plume”, and proposed that this was associated with the higher thermal conductivity of helium. Upon high laser scanning speeds, melt tracks produced on a conventionally manufactured substrate were deeper with helium than with argon.

In this thesis study, results obtained using helium and argon-helium mixtures to process 316L stainless steel and Ti-6Al-4V are reported. In parallel, recent work conducted by Traore et al.⁵⁰ compared the use of argon and helium to produce Inconel 625 parts. Their results agree with those obtained herein, suggesting a positive reduction in the generated spatter under helium. This finding is further developed in the discussion of the results obtained in this thesis.

In addition to helium, the intentional use of oxygen- and carbon dioxide-rich process atmospheres, i.e. 0.2% O₂ and 2% to 100% CO₂ was recently proposed by Haines et al.⁵¹ as a possible new manufacturing route for oxide dispersion strengthened steels, i.e. alloy PM2000. They reported that the oxygen content increased compared to the feedstock powder only when using CO₂ in concentrations of at least 8%. In addition, oxygen loss was observed for higher laser energy densities. The results from compression testing highlighted a yield strength approximately 20% higher for the samples produced in 100% CO₂ compared to argon equivalents, and was attributed to strengthening by the in situ formed oxides⁵¹.

CHAPTER 4

316L STAINLESS STEEL

316L stainless steel is a widely used steel offering a combination of high corrosion resistance and mechanical properties. The high chromium content ensures the formation of a stable protective oxide layer and the high nickel content allows for the stabilization of the austenitic γ face centered cubic (fcc) phase up to its melting point, see typical composition of the alloy in Table 3. Its typical low carbon concentration limits the formation of chromium carbides detrimental to corrosion resistance. The limited number of phases that can form makes it a relatively easy-to-process alloy by L-PBF, and a fully austenitic microstructure is usually obtained in the as-built condition.

Table 3: Chemical composition of 316L stainless steel in wt.% as per ASTM F3184⁵².

Element	Min	Max
Fe	Bal.	
Cr	16.0	18.0
Ni	10.0	14.0
Mo	2.00	3.00
Mn	-	2.00
P	-	0.045
S	-	0.030
Si	-	1.00
C	-	0.030

4.1 Microstructure development and properties

The thermal gradient induced by the laser radiation is perpendicular to the melt pool boundaries, and the melt pool solidifies from its edges toward its centre. The solidification structure resulting from L-PBF for 316L stainless steel is typically cellular. The cell core consists of the austenitic phase, while evidence has been found for the segregation of Mo and Si (ferritic stabilizers) at the cell boundaries. These cell boundaries appear to be favourable sites for the accumulation of dislocations⁵³. The cell size typically varies between 0.3 and 1 μm ^{54,55}, see Figure 13c, and up to hundreds of μm in length, thereby forming a dense dislocation network. The cell size is known to depend on the solidification conditions, namely the cooling rate, the thermal gradient and the velocity of the solidification front⁵⁶. The cells grow along the local thermal gradient and are therefore perpendicular to the melt pool

boundaries. The shape of the melt pool is determinant for the observed orientation of the solidified cells and depends strongly on the laser parameters. Generally, when the melt pool is shallow with a large radius, a strong $<001>$ texture develops, but when it is deeper and its radius decreases, a $<101>$ texture tends to form^{57,58}, see Figure 13b. Grain boundaries are defined by a crystallographic misorientation between cells of at least 10° , which is connected to the local differences in the direction of temperature gradient. Upon the deposition of subsequent layers, a global heat flow along the building direction is established and promotes the epitaxial growth of the grains through several melt pool boundaries. Figure 13 displays the described obtained microstructure for 316L stainless steel produced by L-PBF.

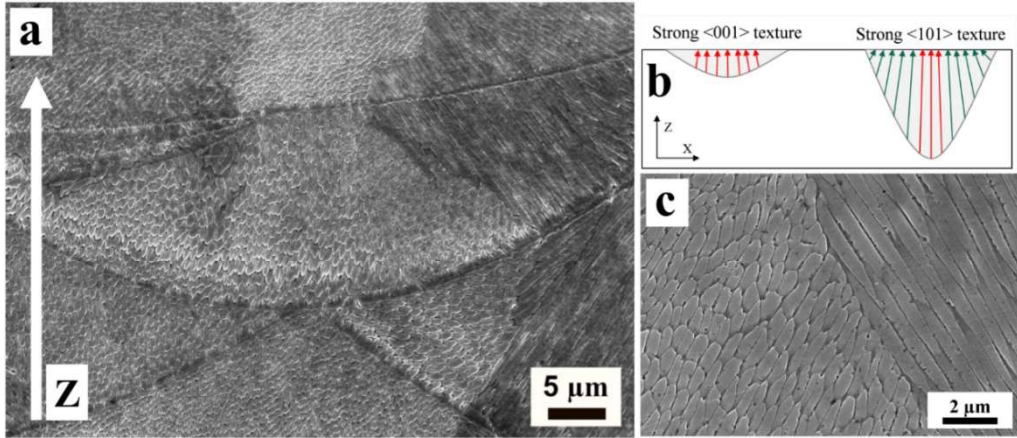


Figure 13: (a, c) Scanning electron micrograph of 316L stainless steel fabricated by L-PBF along the building direction; (b) schematic showing the influence of the melt pool shape on the texture formation.

Because of its fine cellular microstructure, 316L stainless steel built by L-PBF usually achieves strength on the order of two to three times greater than its wrought counterparts, i.e. yield strength of about 550 MPa⁴¹. However, the work hardening is limited with ultimate tensile strength of about 650 MPa⁴¹. In addition, it does not exhibit the common strength-ductility trade-off and generally has high ductility, which can exceed 50%⁵⁹. The dense cell and dislocation network is responsible for this steady work-hardening behaviour, as it is stable up to high strain levels, allowing for dislocations to pile-up⁵³.

4.2 Effect of oxygen and nitrogen

Nitrogen has been added to 316L stainless steel for its austenite stabilization effect and contributes to solid solution strengthening. Nitrogen solubility in austenite decreases with increasing temperatures above approximately 1000 °C⁶⁰. At lower temperatures, it results in nitride formation such as CrN and Cr₂N. As explained by Somers et al.⁶¹, the strong affinity between chromium and nitrogen can lead to elevated meta-stable nitrogen solubility, exceeding amounts that can be bound to chromium or dissolved in austenite, according to thermodynamic predictions. Nonetheless, the possible reduction of chromium in solid solution is potentially harmful to the corrosion resistance. Rawers et al.⁶⁰ calculated the equilibrium nitrogen concentration in Fe-15Cr-15Ni for different nitrogen isobars and reported approximately 0.25 wt.% N in the austenitic matrix at 1 bar of N₂.

The solubility of oxygen in austenite is expected to be low, and the formation of oxide inclusions with Cr, Mn and Si is likely. Kitchener et al.⁶² estimated it to be about 0.003 wt.%.

For oxygen contents above 200 ppm, the Cr₂O₃ and MnO oxides become detrimental to the strength of 316L stainless steel produced by hot isostatic pressing (HIP) since these oxides act as nucleation sites for micro-voids during plastic deformation⁶³. Similar conclusions were drawn for 316L stainless steel produced by L-PBF⁶⁴. In a recent work, Riabov⁶⁵ used nano-sized oxides formed during L-PBF of 316L stainless steel (under argon of high purity) to achieve oxide dispersion strengthening. Some parallel study by Zhong et al.⁶⁶ mixed 316L stainless steel powder to Y₂O₃ powder and reported an interesting combination of high strength, i.e. YS above 570 MPa, and elongation of about 90% at room temperature.

Additional work has compared the influence of the process gas, argon or nitrogen, on the properties of 17-4 PH, a precipitation hardened steel⁶⁷. The results revealed that the austenite stabilization by nitrogen introduced from the process gas was significant for nitrogen atomised powder. The parts produced under argon were mostly martensitic (about 8% austenite), while their nitrogen counterparts exhibited up to 75% austenite. Cheruvathur et al.⁶⁸ also reported the presence of austenite in as-built 17-4 PH stainless steel by L-PBF, which they attributed to both the nitrogen atomizing media and the nitrogen as L-PBF process atmosphere.

CHAPTER 5

ALLOY 718

Alloy 718 is a precipitation strengthened nickel-iron base superalloy, see composition details in Table 4. “Superalloys” refers to a group of high temperature materials designed to sustain high mechanical and chemical resistance up to temperatures close to their melting point. The superalloys have been developed since the 1950s for jet engines and modern aeroplanes still depend on them⁶⁹. The primary strengthening for Alloy 718 is fulfilled by the precipitation of the intermetallic γ'' phase Ni_3Nb of body-centered tetragonal (bct) structure in the austenitic γ phase (fcc) matrix. The excellent properties of Alloy 718 at operating temperatures close to 650 °C are attributed to the coherency strains introduced by γ'' ⁶⁹. Above 650 °C, the orthorhombic and incoherent δ phase becomes thermodynamically stable and precipitates at the expense of γ'' , reducing the materials’ strength^{70,71}. In addition, the presence of Ti and Al is responsible for the smaller presence of the strengthening coherent γ' phase ($\text{Ni}_3(\text{Al}, \text{Ti})$). Other commonly encountered phases are MC carbides (cubic structure), mostly rich in Nb and Ti, and Laves phase⁷² (hexagonal structure). However, the cooling rates during L-PBF are extremely high and the strengthening phases γ'' and γ' are typically not observed in the as-built state. In general, the microstructure of Alloy 718 is highly dependent on the primary manufacturing route and the applied post heat treatments.

Table 4: Chemical composition of Alloy 718 in wt.% according to AMS 5662⁷³.

Element	Min	Max	Element	Min	Max
Ni	50.00	55.00	C	-	0.08
Cr	17.00	21.00	Ta	-	0.05
Fe	Bal.		Co	-	1.00
Nb	4.75	5.50	Mn	-	0.35
Mo	2.80	3.30	B	-	0.006
Ti	0.65	1.15	Si	-	0.35
Al	0.20	0.80			

5.1 Microstructure development and properties

During L-PBF, as the melt pool solidifies, γ dendrites are formed at the melt pool boundaries. Because of the different solubilities of alloying elements in the matrix compared to the liquid, segregation occurs. Nb, Mo, Ti and C with a low solubility in the matrix, tend to segregate to the liquid, while elements like Cr, Fe and Al with higher solubility in the matrix, can be trapped

in the solid. This is typically accompanied by the precipitation of MC carbides and Laves phase in the interdendritic regions, as observed in samples produced by L-PBF⁷⁴.

Similar to cell size for 316L stainless steel produced by L-PBF, the primary dendrite arm spacing (PDAS) can also be connected to the local cooling rate⁷⁵. In general, no secondary dendrite arms grow, and the primary dendrites typically have size about 500 nm, see Figure 14. Similar to 316L stainless steel produced by L-PBF, grain boundaries are defined by larger misorientation between dendrites and grains grow epitaxially along the building direction. Despite the absence of the γ'' and γ' phases in the as-built state, the fine microstructure and high dislocation density confers high tensile strength at room temperature to the material, i.e. YS of about 800 MPa for horizontally built specimens with an elongation of about 30%⁷⁴. The tensile strength can be further increased by post heat treatment thereby achieving YS higher than 1200 MPa but at the expense of elongation⁷⁴. Important effort has been devoted to define the suitable heat treatment to improve the high temperature strength and ductility of Alloy 718 produced by L-PBF⁷⁶.

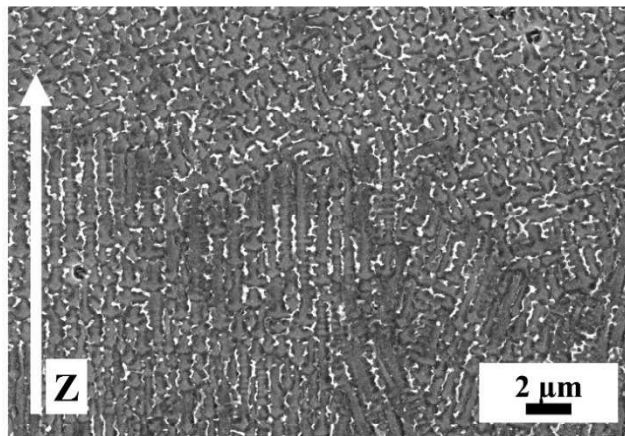


Figure 14: Scanning electron micrograph of Alloy 718 built by L-PBF along the building direction.

5.2 Effect of oxygen and nitrogen

Because of the presence of Ti and Al, characterized by a high affinity to oxygen, it is possible to find stable oxides such as TiO_2 and Al_2O_3 in Alloy 718. A known problem from powder metallurgy (PM) is that oxygen on the surface of the metal particles can lead to the formation of prior particle boundaries (PPBs) decorated with these oxides upon HIP⁷⁷, which is detrimental to the material's strength. For L-PBF, the high temperatures involved with laser melting trigger the oxidation of the 718 spatter generated, as highlighted by Gasper et al.⁷⁸. The authors reported the formation of Al_2O_3 and TiO_2 oxide features on spatter within the range of accepted particle size, which would potentially be re-used and be precursors for oxide inclusions in the produced material.

Nitrogen is known to trigger the precipitation of nitrides of high melting point, which appear in the melt even before the γ phase. The amount of nitrogen dissolved in the melt dictates the amount of formed TiN. Studied by several authors^{79,80}, these precipitates exhibit an hexagonal faceted morphology and are sometimes accompanied by Al- and Mg-rich oxides. In addition, they have been identified as possible preferential nucleation sites for MC carbides. In the context of AM, these nitrides can also be inherited from the feedstock material because of their high melting point of 2930 °C⁸¹.

CHAPTER 6

Ti-6Al-4V

The Ti-6Al-4V is a $\alpha + \beta$ titanium alloy widely used in the aerospace and medical industries as it offers a high strength-to-weight ratio, workability, weldability and biocompatibility, see composition in Table 5. This alloy is therefore one of the first candidates, alongside 316L stainless steel, for L-PBF. At high temperatures it is characterised by the β body centered cubic (bcc) phase, and upon slow cooling below the β transus temperature (approximately 990 °C), it partially transforms into the α hexagonal close packed (hcp) phase. Upon quenching from the β phase field (i.e., cooling rates above 410 K/s⁸²), α' martensite enriched in vanadium may form from the diffusionless transformation $\beta \rightarrow \alpha'$, also of hcp structure with close lattice parameters to that of the α phase.

Table 5: Chemical composition of Ti-6Al-4V in wt.% as per ASTM F2924⁸³.

Element	Min	Max
Ti	Bal.	
Al	5.50	6.75
V	3.50	4.50
Fe	-	0.30
O	-	0.20
C	-	0.08
N	-	0.05
H	-	0.015
Y	-	0.005

6.1 Microstructure development and properties

The high cooling rates associated with L-PBF are responsible for the appearance of the α' martensite of similar structure to the α phase but with the retained composition of the parent β phase. A complete transformation from the parent β phase into fine acicular α' martensite is usually obtained^{84,85}, see Figure 15. The reconstruction of parent β grains using Burger's orientation relationship has highlighted an epitaxial growth of the parent grains along the building direction, similar to the previously presented alloys processed by L-PBF. The scanning electron microscope (SEM) observations of the as-built microstructure reveal a hierarchy within the formed martensite with primary coarser lamellas up to quartic finer lamellas⁸⁵. Furthermore, the high density of dislocations and twins within the martensite

lamellas has been attributed to the accommodation of severe thermal stresses during rapid cooling. Wang et al.³⁹ proposed that these dislocations provide preferential sites for further martensite nucleation and growth upon the subsequent L-PBF thermal cycles and are therefore responsible for the hierarchical martensitic microstructure. In addition, re-heating has been shown to promote the diffusion of vanadium from the supersaturated α' toward the lamellas interfaces. Upon heat treatment, the transformation of martensite to α and the formation of the β phase at the lamellas' interface has been demonstrated. The microstructure formed confers high strength to the as-built material and YS is typically above 1100 MPa, but it is brittle with elongation typically below 10%⁸⁶.



Figure 15: Scanning electron micrograph of Ti-6Al-4V built by L-PBF along the building direction.

6.2 Effect of oxygen and nitrogen

Because of its high content in Ti and Al and their high affinity for oxygen and nitrogen, Ti-6Al-4V can be subjected to significant oxygen and nitrogen dissolution, with solubilities of oxygen up to 22 at.% and nitrogen up to 15 at.% calculated with ThermoCalc. Oxygen in solid solution impedes the movement of dislocations because of their interaction with the lattice strains around the solute atom⁸⁷, resulting in dramatic embrittlement. In addition, oxygen is a strong α phase stabilizer⁸⁸. Nitrogen can also contribute to the solid solution strengthening and form nitrides such as TiN and Ti₂N, which are sometimes used to improve wear resistance. Recent studies have found that the oxygen dissolution during L-PBF of Ti-6Al-4V is detrimental for ductility⁴³. Velasco-Castro et al.⁹⁰ obtained oxygen enrichment for lattice structures by adjusting the scanning strategy, resulting in poor ductility and compressive strength.

CHAPTER 7

DEFECTS CONNECTED TO THE PROCESS ATMOSPHERE

The study of the process atmosphere in this work was conducted primarily by investigating the presence of defects in the L-PBF produced parts. The occurrence of specific types of flaws in relation to the three studied materials and their effect on applications these materials are associated with, are shortly presented in this chapter.

316L stainless steel has applications in many industries, such as medical and automotive. Produced by L-PBF it is generally fully austenitic with no other secondary phases, and possesses high ductility. Therefore producing this steel is relatively straightforward, and it rarely suffers from defects such as cracking. Still flaws connected to insufficient melting, referred to as lack-of-fusion, can occur because of insufficient energy input, non-optimal laser parameters or local powder bed variations⁹¹. The powder bed variations may be connected to the presence of large particles, possibly agglomerated particles or oxidized spatters of different sizes. In addition, the atmosphere's purity is likely to influence the oxidation of the spatters. Oxide inclusions can also be found in 316L stainless steel produced by L-PBF, in sizes ranging from the nano- to the micro-scale, either spherically shaped, see Figure 16a, or irregular and often connected to lack-of-fusion pores. These may represent a threat to the toughness of the produced material. The spherical oxide inclusions may be related to the feedstock powder where they are found in the form of surface oxide features, which may agglomerate in the melt during L-PBF and spheroidize. The gas is likely to play an important role in the mitigation of the mentioned defects through the removal of the spatters and the limitation of their oxidation.

Alloy 718 has been designed for high temperature aerospace applications and is the material of choice for gas turbine discs, which are typically subjected to high temperatures and cyclic loading. This alloy has also been implemented in the nuclear, oil and gas industries⁹². The partitioning of its alloying elements leads to the formation of a segregated microstructure consisting of γ cells, Laves phase, carbides, nitrides and oxides. Similar to 316L stainless steel, lack-of-fusion defects can be found, see Figure 16b and d, and severely affect the fatigue life as they act as crack initiation sites⁹³. In general, HIP is applied to remove porosity in superalloys produced by casting, powder metallurgy⁹² and now AM⁹⁴. Hot isostatic pressing is similar to a heat treatment but is performed under pressure, typically using argon, during which densification occurs mostly by diffusional creep and finally normal diffusion⁹⁵. HIPed material can be subjected to thermally induced porosity (TIP). Typically occurring at elevated temperatures, TIP corresponds to the regrowth of pores under the increasing internal pressure. In addition, materials processed under the vacuum atmosphere used in electron beam melting (EBM) are less susceptible to TIP than their L-PBF counterparts processed under argon⁹⁶. TIP

happens when the pores that disappeared during HIP had only shrunk because of the limited diffusion of the gas trapped in the porosity. The initial gas porosity may come from the atomization of the feedstock powder and be transferred to the as-built material, e.g. the gas bubble being unable to escape the rapidly solidifying melt during L-PBF⁹⁷. Gas pores may also be formed during L-PBF, when interstitial elements have a solubility drop upon solidification for certain alloys. This phenomenon is rather well-known for welding of Al alloys, which are sensitive to the formation of hydrogen pores. The control of the powder handling and the reduction of the adsorbed moisture on the particles' surface has proven beneficial for the mitigation of the generation of these pores⁹⁸. The residual oxygen, hydrogen and moisture during L-PBF processing are also likely to be relevant. In addition, the generation and collapse of a keyhole, as described in Figure 7, can lead to the entrapment of gas cavities^{99,100}. Overall, the type of process gas and the stability of the melt pool could influence the densification during HIP and the later occurrence of TIP in L-PBF components.

Ti-6Al-4V is also widely employed in the aerospace industry, and because of its biocompatibility, it is also used for prosthetic purposes and, combined with L-PBF has great potential for customized implants. In addition, lack-of-fusion defects of distinctive irregular appearance threaten its fatigue properties, see Figure 16c. Compared to 316L stainless steel and Alloy 718, Ti-6Al-4V is more sensitive to oxygen dissolution and embrittlement, and thus the atmospheres' purity is likely to be of primary importance.

Other defects at the scale of the produced component are connected to the L-PBF process, including dimensional deviations associated with a poor calibration of the optical system, residual stress induced distortions, surface defects, roughness from sintered particles, etc.

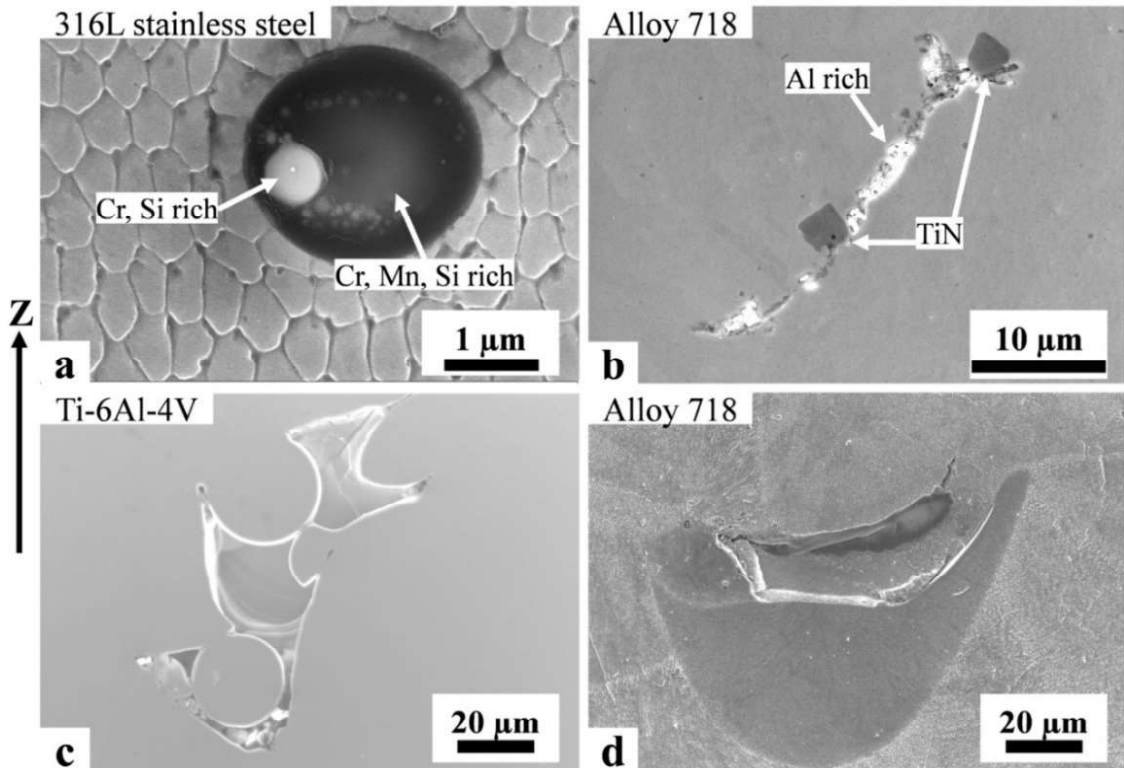


Figure 16: Encountered defects in L-PBF produced materials: (a) Oxide inclusion in 316L stainless steel, (b) oxides and nitrides accumulated around a lack-of-fusion defect in Alloy 718, (c) lack-of-fusion defect in Ti-6Al-4V, and (d) lack-of-fusion defect in Alloy 718 produced with high laser scanning speeds.

CHAPTER 8

EXPERIMENTAL METHODS

8.1 Laser powder bed fusion process

Laser powder bed fusion systems

An EOS M290 (EOS GmbH) machine equipped with an Yb-fibre laser of 400 W maximum nominal power was operated to produce most of the studied materials. This machine features a build area of $250 \times 250 \text{ mm}^2$ with a maximum built height of 325 mm. Samples were built from 316L stainless steel powder supplied by Höganäs AB with particle sizes ranging from 25 μm to 53 μm , using standard (*316L_SurfaceM291 1.10*) and custom parameters. Alloy 718 specimens were produced from powder supplied by Höganäs AB and EOS GmbH with particle sizes ranging from 20 μm to 63 μm , using standard (*IN718_PerformanceM291 2.11*) and custom printing parameters. Finally, Ti-6Al-4V parts were produced using powder supplied by AP&C of Grade 5 with particle sizes ranging from 15 μm to 45 μm , with standard (*Ti64_PerformanceM291 1.10*) and custom printing parameters. Additional printing of Ti-6Al-4V was conducted on an AconityMINI (Aconity3D GmbH) with a baseplate of 100 mm in diameter at Fraunhofer ILT for shadowgraph acquisition. A TruPrint1000 (Trumpf GmbH) of 200 W nominal maximum laser power and 100 mm baseplate diameter and a maximum build height of 100 mm, was also used to produce Ti-6Al-4V samples using powder supplied by Heraeus (Extra Low Interstitial ELI Grade 23) and the machine manufacturer's standard parameters (*TruPrint_1000_Spot30_Ti64_ELI-A_Surface_v2.0*).

Oxygen monitoring

To analyse and control the residual oxygen in the process atmosphere, an external monitoring system was used: the ADDvance® O₂ precision, developed by Linde GmbH, see Figure 17. This system samples about 1 L/min of the process atmosphere close to the build area, analyses it using a lambda probe, an electrochemical cell and a dew point analyser, and returns it. The system can adjust the process atmosphere's purity if the operator selects a set point. Purge gas (argon or nitrogen) is used to flush the electrochemical cell when in standby to prolong its lifetime.

Typically the achieved L-PBF atmosphere purity is dependent on many factors including machine, oxygen sensor types, calibration and gas supply quality. In this work on a medium size machine equipped with an electrochemical cell (EOS M290), a residual oxygen level between 400 to 800 ppm O₂ was measured using high quality argon and nitrogen (less than 10 ppm impurities), and following standard calibration and purging procedures, to process 316L

stainless steel. As the gas impurity level increases, the achieved process atmosphere is impaired when following a systematic purging procedure. This was highlighted by a recorded level of 2000 ppm O₂ when using the nitrogen delivered by a generator that filtered compressed air.

Monitoring the atmosphere established on a smaller sized machine (TruPrint1000) demonstrated that the oxygen sensor type is critical for the purity achieved during L-PBF. A lambda probe, commonly used in the automotive industry, can lead to important underestimation of the actual oxygen level because of the presence of hydrogen molecules in the process atmosphere. Such a cross-sensitivity of the lambda probe was put in evidence by a parallel recording of the oxygen by an electrochemical cell and a lambda probe. The results revealed an increase of about 700 ppm of O₂ during a 7 h print when controlling with a lambda probe. Controlling with an electrochemical cell achieved stable levels down to 100 ppm O₂ and below. The definition of the appropriate residual oxygen level in L-PBF process atmosphere has to be made in regard to the processed materials.

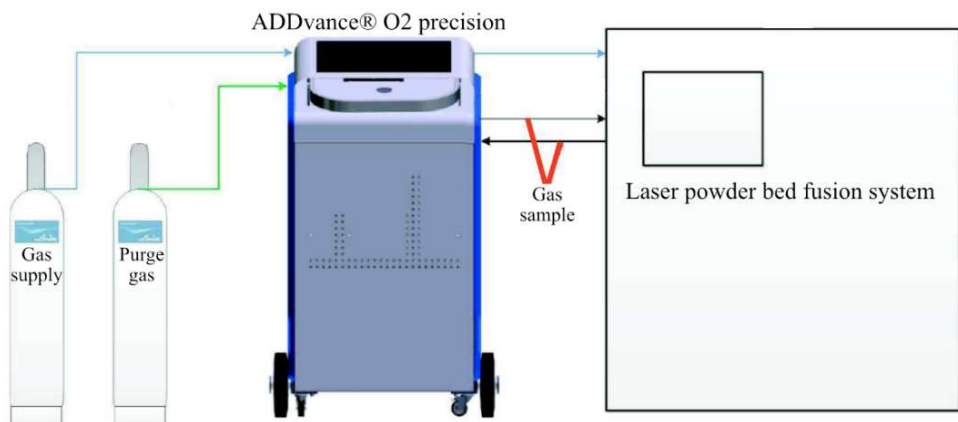


Figure 17: ADDvanceO2® precision system used to monitor the residual oxygen in the process atmosphere (Source: Linde GmbH).

Process gases

Different gases and starting purities were investigated, ranging from high purity technical gases to lower purity nitrogen, as detailed in Table 6. The figure following the gas name specifies its purity: 5.0 means the purity is at least 99.999%, and 4.6 corresponds to a purity of at least 99.996%. In addition, the mixtures employed had purities of at least 99.999%.

Table 6: List of the gases and their properties employed in this work. The properties are given at NTP (normal temperature and pressure: 20 °C and 1 atm) (Source: Wolfram-Alpha curated data, 2020). The specific heat capacities of the gas mixtures were calculated using respective mass fractions and specific heat capacities. The listed ranges of thermal conductivity for the mixtures were reported from experimental work.¹⁰¹

Gas	Density [kg/m ³]	Specific heat capacity at constant pressure [J/(kg·K)]	Thermal conductivity at 25°C [W/(m·K)]
Argon 5.0	1.62	522	0.018
Nitrogen 5.0	1.14	1041	0.025
Helium 4.6	0.16	5193	0.154
VarigonHe50 ¹	0.89	942	0.040 to 0.070
VarigonHe30 ²	1.18	709	0.020 to 0.040

¹ 50% He, 50% Ar

² 30% He, 70% Ar

8.2 Material characterization

8.2.1. Metallographic preparation

Powder samples for the investigation of powder morphology were prepared by slight powder pressing into small and soft metallic plates (approximately $5 \times 10 \text{ mm}^2$), either of pure Al or In. Samples for microstructure investigations were mounted in conductive resin, ground and polished using Struers hardware until a mirror finish was achieved.

The 316L stainless steel and Alloy 718 samples were electrochemically etched in a 10 vol.% oxalic acid using a platinum counter cathode with potentials of 3V and 6V respectively. Since electrochemical etching appeared unfeasible to reveal the microstructure of the Alloy 718 powder and spatter cross-sections, these were instead chemically etched by swabbing with Kalling's No. 2 reagent (5 g CuCl₂, 100 mL hydrochloric acid and 100 mL ethanol). The Ti-6Al-4V samples were chemically etched with Kroll's reagent (92 mL water, 6 mL nitric acid and 2 mL hydrofluoric acid).

8.2.2. Imaging techniques

Light optical microscopy

Leitz DMRX and ZEISS Axioscope 7 microscopes were used for investigating the polished cross-section of samples. Porosity measurements were conducted by image analysis using the freeware ImageJ. Microstructural characterization was performed on etched specimens.

Scanning electron microscopy

Powder morphology, microstructural features and fracture surfaces were studied using the signal from the secondary electrons (SEs) collected by the in-lens detector in a LEO Gemini 1550 (LEO GmbH) SEM.

In SEM, a beam of electrons generated by a source, in this work a field emission gun, and accelerated to a potential of several keV, was focused and rastered on the sample surface using several electromagnetic lenses. The incoming electrons interact with the targeted sample, generating different signals that can be detected and employed for the sample's characterization, see Figure 18. The size of the generated interaction volume is in the range of several micrometres and varies depending on the energy of the incoming electrons, the material studied and the incidence angle¹⁰².

Secondary and backscattered electrons are usually employed for imaging purpose. The SEs originate from the ionization of the atoms of the specimen, i.e. inelastic scattering of primary electrons, and typically have low energy (below 50 eV), and thus only the SEs generated close to the sample's surface can escape and be detected. Therefore, this signal provides topographic contrast. The backscattered electrons (BSEs) are a result of the elastic scattering of the primary electrons and are thus more energetic and can escape and provide information from deeper volumes of the sample. In addition, the BSEs yield increases for heavier elements which appear brighter than lighter elements, and thus the collected signals offer chemical contrast. Finally, ionized atoms release excess energy to restore their original configuration by transfer of outer

shell electrons to lower energy positions. This release of energy leads to the emission of X-ray photon of characteristic energy, which is seen as a specific line on the X-ray spectrum. The energy of the emitted X-ray photon depends on the difference in energy between the shell with the void and the shell from which the filling electron originates. Therefore, the collection of this signal during energy-dispersive X-ray spectroscopy (EDS) provides chemical information.

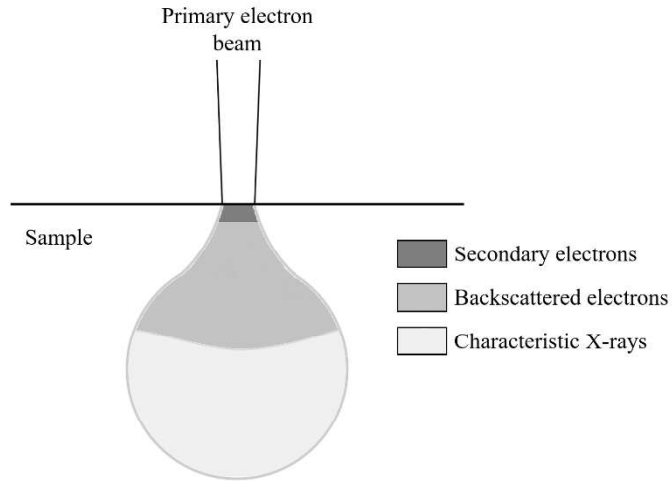


Figure 18: Schematic of the interaction of the incoming electron beam with the sample, highlighting the studied signals during SEM.

In addition, electron backscattered diffraction (EBSD) was also conducted with a Nordlys II detector (Oxford Instruments) to obtain crystallographic information from the 316L stainless steel and Ti-6Al-4V material produced in this work. EBSD exploits diffraction patterns resulting from the interaction of the primary electrons with the crystalline sample.

X-ray computed microtomography

X-ray computed microtomography (XCT) allows one to conduct quantitative analyses of different defects, such as porosity in the volume of L-PBF-produced materials, including distribution, size and morphology, in a non-destructive manner. In addition, XCT permits the construction of a 3D representation of the object with algorithms, using projections around this object with X-rays, see Figure 19. The contrast of the recorded projections is based on the attenuation of X-rays passing through the object, which depends on the material's density and its atomic number. The reconstructed volume is composed of voxels equivalent to volumetric pixels. Less accessible and more expensive, synchrotron-based XCT (SXCT) offers the highest resolution thanks to the high brilliance of the X-ray source, which grants high signal-to-noise ratio and sub-micron voxel resolution^{103,104}. It is typically performed on small-sized specimens, e.g. cylinders of 1 mm in diameter.

The XCT measurements on Ti-6Al-4V specimens (of geometry $1 \times 5 \times 15 \text{ mm}^3$ and $5 \times 5 \times 15 \text{ mm}^3$) were conducted at the Federal Institute for Materials Research and Testing (BAM, Berlin, Germany) with a v|tome|x L 300 CT system from General Electric. Finally, SXCT measurements were performed at the BAMline, BESSY II (Berlin) for accurate pore morphology reconstruction, see Paper IX.

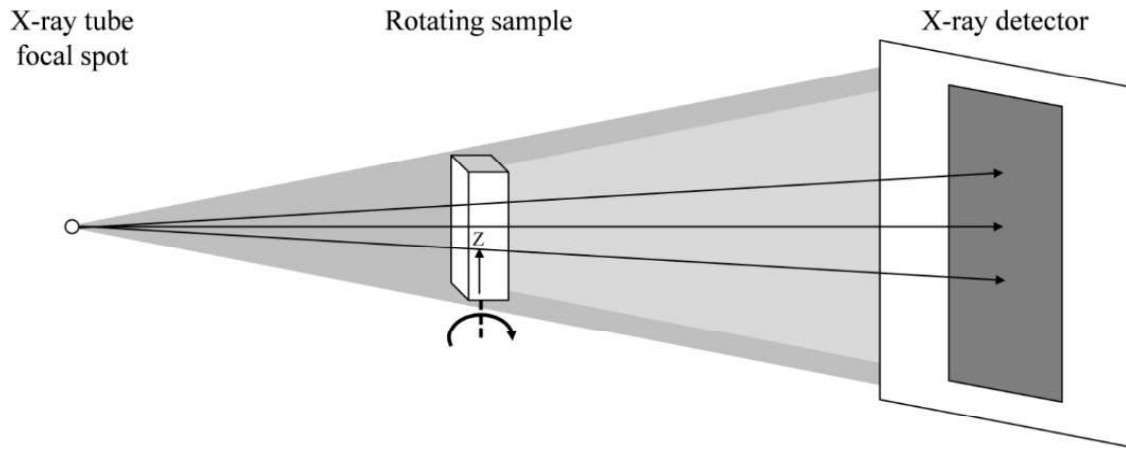


Figure 19: Schematic diagram of a laboratory X-ray computed microtomography set-up, redrawn from Cnudde et al.¹⁰⁵

8.2.3. Non-imaging techniques

Chemical analysis

The chemistry of powder and bulk samples was measured by combustion gas analysis for the light interstitial elements (C, O and N) using a LECO ON836 and CS844 at Höganäs AB, and a LECO ONH 836 at Linde GmbH. The samples are weighted and placed into a graphite crucible, which is introduced into a furnace section, where it melts and releases gases. Helium gas carries these produced gases toward a series of sensors. The oxygen from the sample reacts with carbon from the crucible and forms CO and CO₂. The CO is oxidized into CO₂, similar to the hydrogen from the sample that forms H₂O. Since CO₂ and H₂O absorb infrared radiation at unique wavelengths, they are detected using non-dispersive infra-red cells (NDIR). Nitrogen is detected using a thermal conductivity sensor (resistive filament).

Hardness

The Vickers hardness of the material produced in this work was measured with a DuraScan (Struers) system using 10 kgf and 1 kgf loads on a polished cross section. This technique measures the material's resistance to local plastic deformation induced by a square base pyramid indenter with a 136° angle. The present system measures the diagonals of the pattern left after indentation and automatically calculates the hardness following relationship:

$$HV = \frac{L}{A} = \frac{2 \sin\left(\frac{136^\circ}{2}\right)L}{d^2} = \frac{1.8544 L}{d^2}$$

where L is the load applied, A is the area of indentation, and d is the average of the two diagonals of the indentation.

Mechanical testing

Samples of 316L stainless steel were built to the net-shape on the EOS M290 horizontally for Charpy impact testing according to ASTM E23¹⁰⁶ and for tensile testing according to ASTM B925-15¹⁰⁷. These samples were first stress-relieved at 300 °C for 2 h and removed from the plate, and the V-notch was machined. They were then tested at room temperature at Höganäs AB.

In addition, other 316L stainless steel net-shaped tensile samples were produced according to ASTM E8/E8M-15a¹⁰⁸ and of a smaller cross-section within the gauge length to study the possible effect of heat accumulation. These samples were tested in the as-built condition at room temperature at Chalmers University of Technology, with an Instron 5500 machine. Clip-on extensometers were used, and the tests were performed under strain rate control at 0.025%/s.

Samples of Ti-6Al-4V were produced on the EOS M290 net-shaped horizontally for Charpy impact testing according to ASTM E23¹⁰⁶ and for tensile testing according to DIN 50125 Form B¹⁰⁹. These were first stress-relieved in vacuum at 650 °C for 3 h and removed from the plate, and the V-notch was machined. Furthermore, Ti-6Al-4V samples produced with the TruPrint1000 were stress-relieved in vacuum at 800 °C for 2 h and machined according to DIN 50125¹⁰⁹. These samples were tested at room temperature in a certified German laboratory (GWP, Dillingen), following the standard procedure DIN EN ISO 6892-1¹¹⁰.

X-ray diffraction (XRD)

X-ray diffraction was conducted on the Alloy 718 and the Ti-6Al-4V specimens produced with the EOS M290 and the TruPrint1000 systems for phase distribution analysis. X-rays are electromagnetic waves of small wavelengths, and thus high energy, in the range of 0.5 to 2.5 Å, allowing them to diffract when passing through a crystal lattice. The principle of the XRD measurement is based on Bragg's law, see Figure 20:

$$n\lambda = 2dsin\theta$$

where n is the diffraction order, λ is the wavelength of the X-ray radiation employed, d is the interplanar distance, and θ is the diffraction angle.

In this work, XRD for phase analysis was performed with a Bragg-Brentano θ/θ configuration, see Figure 20. In other words, the X-ray source and detector move along an arc with the same angular speed. Phase identification is performed by identifying the angles (θ) at which constructive interference of X-rays occurs (intensity peaks) and converting these angles into interplanar distances (d). The observed sets of peaks can then be matched to standard diffraction patterns from the PDF database (Powder Diffraction Files). From the interplanar distances and considering the studied system, lattice constants are derived, for example, for cubic lattice (e.g., Ti-β) as follows:

$$\frac{1}{d_{hkl}^2} = \frac{h^2 + k^2 + l^2}{a^2}$$

Or for hexagonal lattice (e.g., Ti- α) as follows:

$$\frac{1}{d_{hkl}^2} = \frac{4}{3} \left(\frac{h^2 + hk + k^2}{a^2} \right) + \frac{l^2}{c^2}$$

where hkl are the Miller indices.

Different X-ray sources were employed to limit the effect of fluorescence, which occurs when the incoming X-rays excite atoms from the studied samples resulting in subsequent X-ray emission. When these X-rays have a wavelength close to that of the source, they are detected and increase the background of the diffraction patterns. Typically, a Cr source is avoided for Ti alloys, as is Cu for Fe-based alloys.

For Ti-6Al-4V and Alloy 718 samples, the system used was a PANalytical X'Pert PRO diffractometer with a Cu K α radiation ($K\alpha_1$ wavelength 1.54056 Å) operated at 45 kV and 40 mA located at Höganäs AB. The Ti-6Al-4V and the Alloy 718 materials were analysed in the 30° to 85° and 30° to 100° ranges, respectively. In addition, XRD was also performed on 316L stainless steel on a Bruker AXS D8 Advance instrument equipped with a Cr source ($K\alpha_1$ wavelength 2.28970 Å) operated at 35 kV and 40 mA in the 30° to 140° range, located at Chalmers University of Technology.

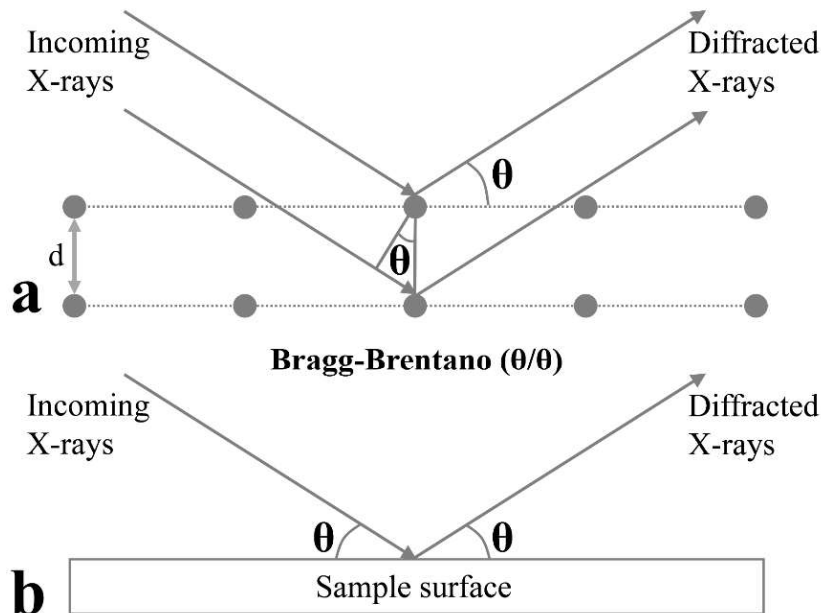


Figure 20: Schematic representations of (a) X-ray diffraction principle and (b) the Bragg-Brentano θ/θ configuration.

Subsurface residual stress measurement

The assessment of subsurface residual stress of L-PBF produced samples is based on the measurement of lattice strains using energy-dispersive diffraction of X-rays, using the $\sin^2 \psi$ method for a reflection setup with a fixed diffraction angle 2θ of 16°. This technique was used to analyse Ti-6Al-4V samples, and the {103} $_{\alpha}$ diffraction peak was used to determine the residual stresses along the building direction Z. Figure 21 is a schematic representation of the measurement setup on a cuboid sample. The measurements were performed at different sample heights for the same surface. In this study, the measurements were conducted with the

laboratory energy dispersive diffractometer (EDD) LIMAX-160 at the Helmholtz Zentrum Berlin by T. Mishurova and her colleagues at the Bundesanstalt für Materialforschung und Prüfung (BAM). The hard X-rays were generated from a continuously flowing liquid Ga-rich alloy anode (with a melting point close to room temperature), with a MetalJet source (Excillum), of K α emission energy of 9.2 keV relatively close to that of Cu (8 keV). The white bremsstrahlung spectrum (up to 160 keV) allowed for the energy-dispersive experiment.

Using the energy dispersive diffraction technique, the signal from crystallographic planes at different energies was recorded, according to Bragg's law and the energy equation ($E = h \cdot c / \lambda$):

$$d^{hkl} = \frac{6.1999}{\sin \theta} \frac{1}{E^{hkl}}$$

where d^{hkl} is the interplanar distance of the planes of family $\{hkl\}$ in Å, θ is the diffraction angle, and E^{hkl} is the energy corresponding to the diffraction of the planes of family $\{hkl\}$ in keV.

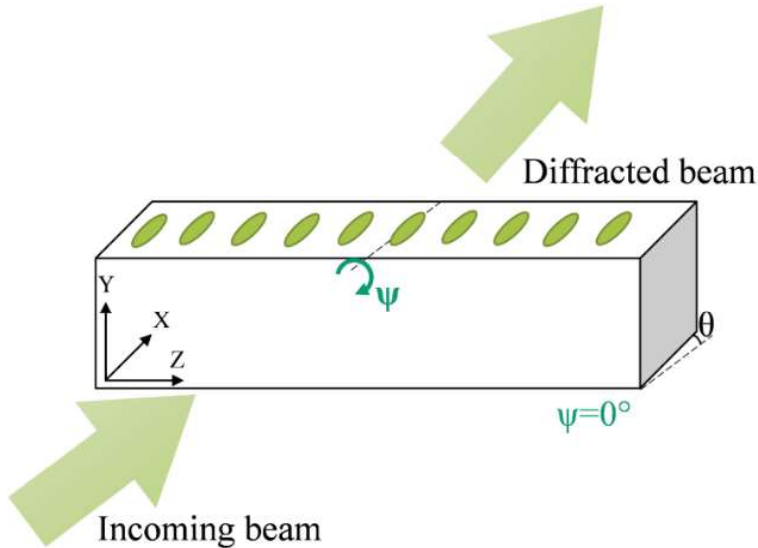


Figure 21: Schematic of the measurement setup. The Z axis corresponds to the building direction, and the green ellipses on the sample surface highlight the measurement points, redrawn from Mishurova et al.¹¹¹

X-ray photoelectron spectroscopy

X-ray photoelectron spectroscopy (XPS), also referred to as electron spectroscopy for chemical analysis (ESCA) is a surface analysis technique based on the ejection of core level electrons from the studied material by X-ray photons of energy $h\nu$. The kinetic energy E_B of these emitted photoelectrons is analysed with a spectrometer. It depends on the X-ray photon energy $h\nu$, on the spectrometer work function W , and on the binding energy of the electron E_B , following relationship:

$$E_B = h\nu - E_K - W$$

The binding energy of the electron is characteristic of the emitted electron and allows its parent element and energy level to be identified¹¹². The recording of a survey spectrum allows identification of the elements present on the surface analysed in a relatively short acquisition

time, while high-resolution scans over selected energy regions for the elements of interest provide chemical state information. Ion etching using Ar^+ allows one to analyse variations at several depths from the as-received surface.

In this thesis, XPS analysis was conducted on the as-built Ti-6Al-4V surfaces of columns produced under different atmosphere purities using a PHI 5500 system (Perkin Elmer, Waltham, Massachusetts, USA). The samples were introduced in the analysis chamber where the pressure was about 10^{-9} mbar. A monochromatic Al K α ($h\nu = 1486.6$ eV) source was used to produce photoelectrons from an area of roughly 0.8 mm in diameter. The energy calibration using Au 4f_{7/2} (84.0 eV), Ag 3d_{5/2} (368.3 eV) and Cu 2p_{3/2} (932.7 eV) was performed prior to the measurements. XPS measurements were conducted by A. Raza on Alloy 718 powder particles to study their degradation in relation to the L-PBF process atmosphere's purity.

8.3 Process characterization

Process snapshots

Process snapshots were taken early in the study of helium's addition to the process atmosphere for Ti-6Al-4V to highlight differences in incandescent spatter generation. A Canon PowerShot SX50 HS camera was placed on a tripod in front of the window of the process chamber of the EOS M290. The exposure time was set to 1/20 s with an ISO speed of 800, without additional illumination of the build area.

Shadowgraphy

Shadowgraphy experiments were conducted at Fraunhofer ILT (Aachen, Germany) on an AconityMINI machine. This technique is based on illumination of the L-PBF process plane from one side and recording the shadow of objects in this plane using a high speed camera. It is a valuable tool to probe metal vapour and spatter generation during L-PBF processing and was used to study Ti-6Al-4V with different process gases.

Two windows were placed on either side of the build area. Outside these windows, opposite to each other, an LED collimated illumination and a high-speed camera (VEO640L, Vision Research) were placed, which recorded the shadowgraphs at a frequency of 10 kHz and an exposure time of 5.13 μs with a resolution of 896×500 pixels. The image recordings were performed during 3 cm long single track experiments using a laser power of about 200 W and a scanning speed of 1000 mm/s. The analysis of the images was performed using ImageJ with the help of the tracking tool TrackMate¹¹³ to quantify the number, displacement, ejection angle and speed of the bright spatter.

CHAPTER 9

RESULTS AND DISCUSSION

9.1 Residual oxygen in the process atmosphere

Effect of atmosphere purity of L-PBF on 316L stainless steel

316L stainless steel parts were produced under argon with different oxygen levels, either monitored by the L-PBF machine or externally from 20 to 800 ppm O₂. Despite the wide range of oxygen levels tested, a limited effect was observed on the density, microstructure, composition and strength of the produced 316L material. This was also verified under high purity nitrogen atmospheres. On the one hand, an important oxygen loss of about 150 ppm (i.e., 25%) was measured when comparing the composition of the feedstock virgin powder to that of the as-built bulk material. Meanwhile such findings were also reported by other authors for 316L stainless steels manufactured by L-PBF. This result is commonly attributed to the dissociation of surface oxides and desorption of oxygen molecules on the metal particle surfaces upon laser heating. As suggested by the pronounced oxidation state of spatter particles, a transfer of this oxygen to the hot ejected melted spatters occurs. On the other hand, nitrogen appears to be mostly transferred from the powder to the built material, which is likely connected to its presence in the bulk of the material.

Processing under lower purity, at 2000 ppm O₂ (measured, machine setup at 10000 ppm) with the nitrogen generator, led to a higher oxygen level of 50 to 100 ppm in comparison to using high quality nitrogen. This result suggests a less important oxygen loss at higher oxygen partial pressures. However, this did not negatively affect the material's properties, which appeared mostly unchanged when using virgin powder. The extent of oxygen uptake during L-PBF processing is most likely hindered at lower oxygen partial pressure because of the rapid solidification, and hence limited kinetics. However, significant powder degradation was observed and hence negative impact on the properties of the components produced using re-used powder can be expected.

The fracture surface analysis of the Charpy impact specimens produced using the nitrogen generator (~2000 ppm O₂) revealed the presence of defects larger than 20 µm, see Figure 22c. Their morphology suggests that they are connected to lack-of-fusion defects, which may have arisen, for example, from the presence of oxides transferred from spatter particles. This was thought-out considering the study of metal particles exposed to the process atmosphere, which highlighted the pronounced oxidation of the powder processed under the nitrogen generator, see Figure 22a and b. Oxide features rich in Cr and Mn and with traces of Si appeared to decorate their surface, see Figure 22b, and may have acted as potential lack-of-fusion or inclusions precursors when close to the melt pool, compromising the component's integrity and possessing high risk of defect formation upon their re-use during L-PBF processing.

Finally, the composition of these surface oxides is in strong agreement with that of the evenly distributed spherical oxides observed on the fracture surface of tensile specimens, pointing out their origin and relative stability during L-PBF processing, which is connected to the high thermodynamical stability of these oxides. The formation of these spherical oxides is assumed to originate from an agglomeration of powder surface oxides and their spheroidization occurring to reduce surface energy during the melt pool lifetime.

Finally, the component design of high aspect ratio, which promotes heat accumulation, also led to enhanced oxygen pick-up by the part, with additional 30 to 50 ppm O₂ in the 1 mm thick gauge vertical tensile specimen compared to their 3 mm thick counterparts. However, the noted reduction of mechanical properties of the 1 mm thick samples was connected to a size effect and surface roughness rather than to the composition difference.

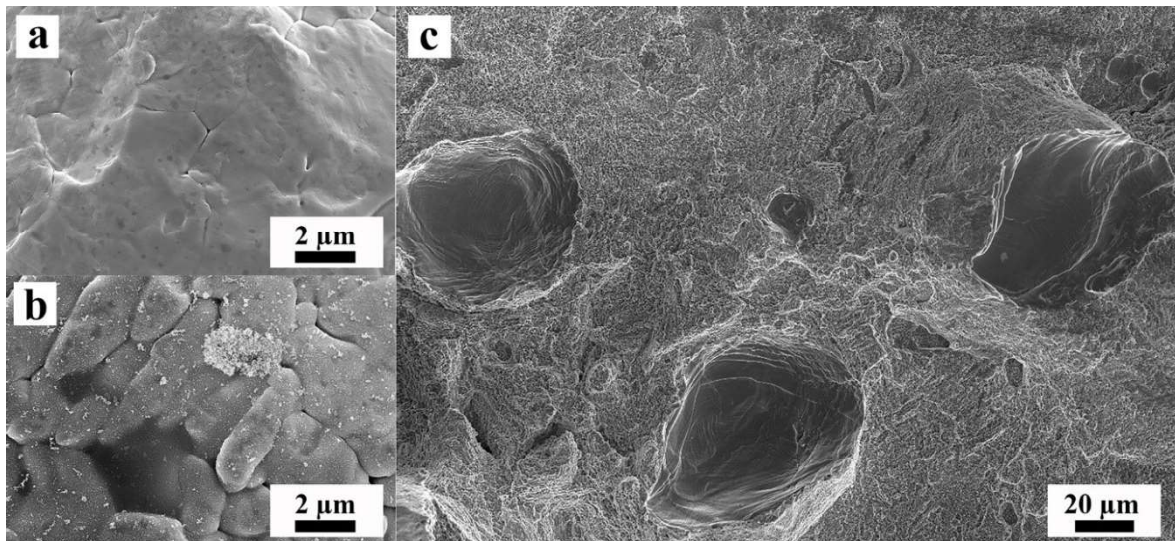


Figure 22: SEM micrographs of the surface of 316L stainless steel powder particles: (a) Exposed to high purity argon, (b) nitrogen produced from the L-PBF machine's internal generator during L-PBF, and (c) fracture surface of a Charpy impact specimen produced with nitrogen from the internal generator and displaying large dimples.

Alloy 718 and oxygen balance

Similar to the previous observation for 316L stainless steel, L-PBF of Alloy 718 led to a significant reduction in oxygen content when comparing the composition of the feedstock powder to that of the as-built material, approximately 30 ppm or 10% in Paper II and up to 160 ppm or 30% in Paper VI, and was attributed to similar causes. Several atmosphere purities were investigated from 50 to 500 ppm O₂ (Paper VI) and standard (Paper II), which all permitted the production of high density Alloy 718 samples with compositions that did not vary significantly.

Based on the 316L stainless steel findings, an in-depth investigation of the oxidation of the exposed powder bed and the generation of spatters was conducted. The cross-section of spatter particles highlighted difference in thermal history compared to the atomized virgin particles. The measurements of the PDAS established that the direct melt pool spatters cooled faster (10^8 K/s) than the produced material (10^7 K/s) and feedstock powder during atomisation (10^6 K/s). The spatters were also composed of agglomerates and to a great extent of entrained particles, which may or may not have interacted with the laser beam on the course of their trajectory, and thus whose PDAS were similar to that of virgin particles. The spatter landing

on the gas inlet, and hence travelling against the gas flow, were mostly composed of large entrained powder particles ($> 80 \mu\text{m}$ in diameter) with high kinetic energy.

The chemical analysis of the powder samples suggests that the oxygen pick-up is enhanced in the order of tens of ppm by the accumulation of spatter particles in the powder bed, for instance in the capsule designed with lattice structures. The oxygen pick-up of the collected spatter particles was in general doubled compared to the virgin particles, while the nitrogen only increased by a few ppm. The greatest oxygen pick-up was measured by combustion analysis for the spatter collected in the gas outlet. The EDS and XPS analysis of the virgin powder, the powder from the bed and the spatter samples indicated the presence of two oxide types, Al- and Cr-rich.

Mitigation of Alloy 718 spatter oxidation

This work was completed with a study of the impact of the residual oxygen level on the oxidation of spatter that landed on the gas inlet and were previously shown to be similar to the spatter collected in the outlet, which experienced oxygen pick-up during high temperature travel in the vicinity of the melt pool. The results highlight a gradual increase in the oxygen pick-up in agreement with the registered increase in the Al-rich and Cr-rich oxide coverage and oxide particulate thickness with increasing oxygen partial pressure, see Figure 23. The measured particle size of the studied spatter confirms that these spatter particles would be contained within a recycling loop. The effect of the blending of this spatter with virgin powder on the properties of Alloy 718 components still needs to be addressed, possibly by studying high temperature and dynamic properties for this alloy, typically used for aerospace high temperature applications.

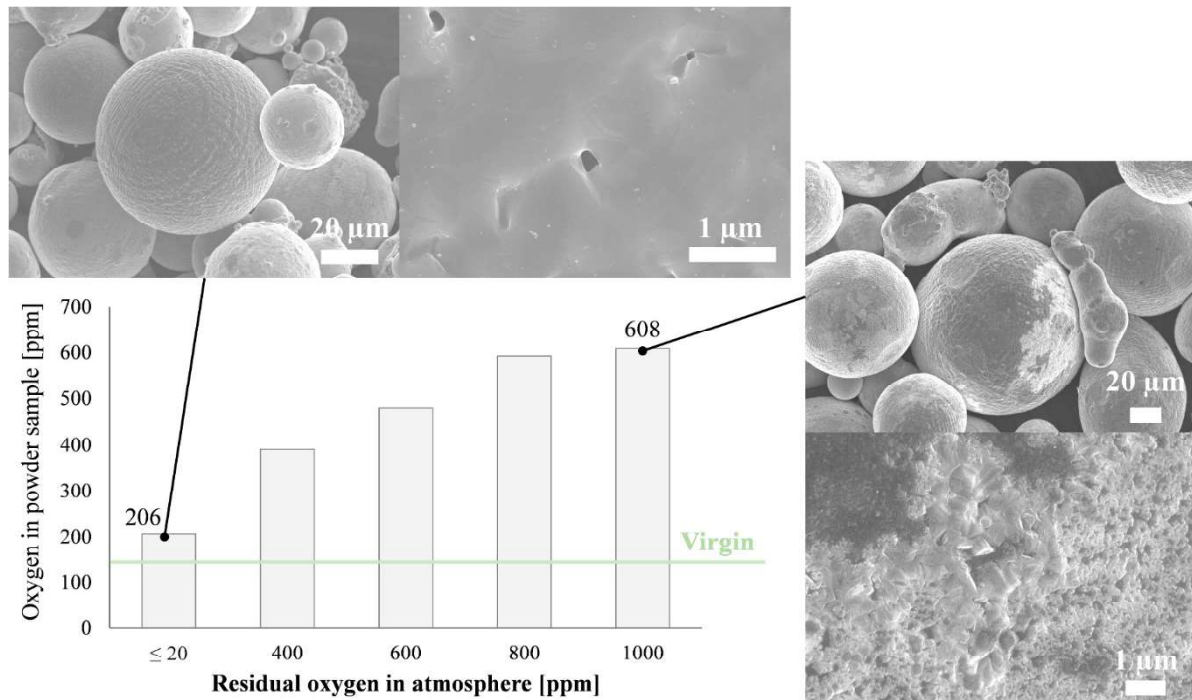


Figure 23: Variation of the oxygen content measured in the Alloy 718 spatters as a function of the residual oxygen in the process atmosphere. SEM micrographs of the surface morphology of 718 spatters exposed to below 1 ppm and 1000 ppm O₂ are displayed.

High sensitivity of Ti-6Al-4V to atmosphere purity

On the industrial scale L-PBF system using an EOS M290, processing Ti-6Al-4V under standard operating conditions without external monitoring did not show effect of the oxygen monitoring on the composition and mechanical properties of the produced samples, indicating good control over the oxygen content by the system. However, a slight relative porosity increase between 0.01% and 0.05% over a wide parameter window was reported and associated with the presence of lack-of-fusion defects. Similar to 316L stainless steel and Alloy 718, spatters were identified as potential carriers for the oxygen enrichment, oxide inclusions and lack-of-fusion defects. A considerable pick-up of about 1000 ppm O₂ and 384 ppm N₂ by Ti-6Al-4V spatters compared to the virgin powder composition was measured after processing under standard conditions. Al-rich fine particulates were identified on the spatter particles, see Figure 24d.

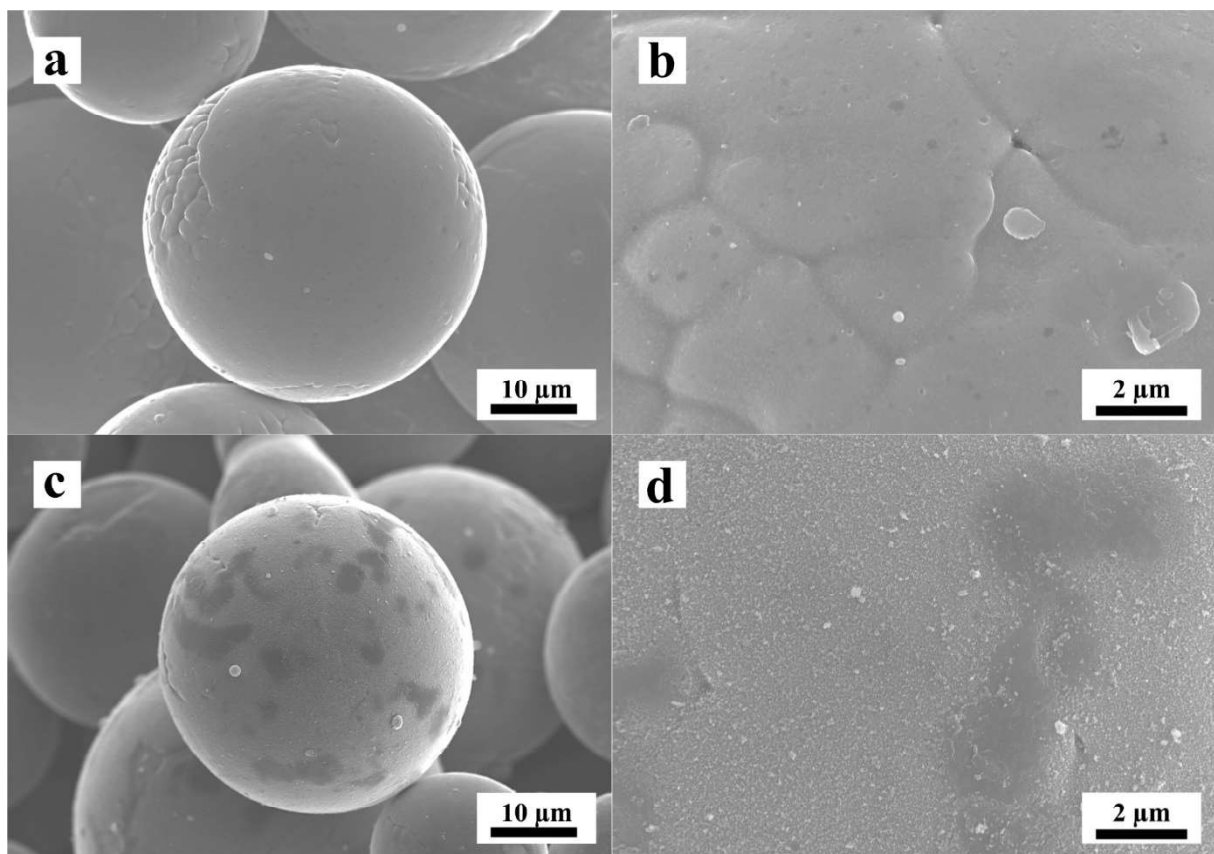


Figure 24: (a-b) Ti-6Al-4V feedstock powder; (c-d) collected Ti-6Al-4V spatter in the gas outlet after L-PBF under argon.

On the laboratory scale set-up (TruPrint1000), important deviations of oxygen levels in the processing gas measured by the machine and by the external system were obtained, leading to an important underestimation of the actual atmosphere purity, critical for the quality of the Ti-6Al-4V components produced as such because of the high affinity of Ti and Al for oxygen. Major oxygen and to some extent nitrogen pick-ups, were measured along the height of columns with dimensions of 70 mm in height and 22 mm in diameter. These composition differences were connected to both, heat accumulation occurring in the high aspect ratio design and the presence of impurities in the process atmosphere. Maximum oxygen and nitrogen

contents were measured at the top of the columns and were 2200 ppm and 500 ppm respectively, for the column produced under standard conditions. This result is 400 ppm O₂ (almost 20%) and 250 ppm N₂ more than when ensuring an oxygen partial pressure of 100 ppm O₂ through the 7 h builds. The oxygen pick-up was also associated with a non-negligible reduction of the ductility with an elongation drop of 4% to 5% between the samples printed close to the baseplate and at a 63 mm height. In addition, significant differences in the surface state of the produced columns was observed by SEM and XPS and is attributed to the development of a few micro-meter thick oxide layer, also rich in nitrogen. Overall, the results highlight the high sensitivity of Ti-6Al-4V to the L-PBF environment and an important reliance on the hardware and oxygen monitoring used.

9.2 Gas type

Alternative use of nitrogen for Fe- and Ni-based alloys

Processing under high purity nitrogen instead of argon for 316L stainless steel yielded similar mechanical properties, and the nitrogen pick-up was only limited, i.e. few tens of ppm N₂ picked-up, see Paper I. This small composition difference did not influence the strength of the L-PBF-produced material, which is mostly driven by the pinning of dislocations by the fine cellular network, and appeared to be of similar size in argon and nitrogen, see Paper X.

For Alloy 718, no pick-up of nitrogen was observed for all studied process atmospheres. Under argon, see Paper II, the nitrogen content remained unchanged during L-PBF when comparing the feedstock powder and the built part (66 ppm N₂). In Paper VI, the feedstock powder used was richer in nitrogen (about 1500 ppm N₂), and processing under both argon and nitrogen was accompanied by an important loss of nitrogen (at least 25%). It was pointed out that the resulting nitrogen content in the samples produced under nitrogen was only slightly higher than in their argon equivalent (about 50 ppm, 5%). This finding was supported by the calculated theoretical increasing nitrogen equilibrium concentration with nitrogen partial pressure. This slight nitrogen increase in the nitrogen sample was not reflected in differences in the nitride population of the built specimens compared to argon ones. Thermodynamic and kinetic considerations highlighted the low solubility of nitrogen in the matrix and the limited precipitation and growth of nitrides permitted upon L-PBF, suggesting that all the observed precipitates are effectively transferred from the powder to the built material. In addition, an important accumulation of nitride and oxide inclusions at the top of the last deposited layer was observed. The mechanical response of the samples should be evaluated, including heat treated state, typically performed to precipitate the strengthening phases.

Use of helium for 316L stainless steel and Ti-6Al-4V

Using standard laser parameters on an industrial scale system and adjusted differential pressure allowed to achieve high density with helium, comparable to that obtained with argon for the tested materials in case of both, 316L stainless steel and Ti-6Al-4V.

For 316L stainless steel, finer cell size was measured for the helium samples, both for the 1 and 3 mm thick tensile specimens, than for their argon and nitrogen counterparts, despite the important standard deviation. This cell size reduction was connected to the enhanced local cooling of the deposited material at the melt pool scale. This slight difference was not reflected in the material's mechanical response, and the samples produced under the three tested gases exhibited overall comparable grain size factors and textures.

For Ti-6Al-4V, laboratory XCT highlighted an increased porosity in the contour areas of Ti-6Al-4V samples produced with helium, see Figure 25, which may be connected to an increased denudation because of the higher emission speed of the generated metal vapours. However, denudation during printing of these samples was not clearly identified and is not suspected with the intermediate argon-helium mixtures. The noted porosity peak close to the sample's edge regardless of the process atmosphere is attributed to a poor overlap of the in-fill and contour regions.

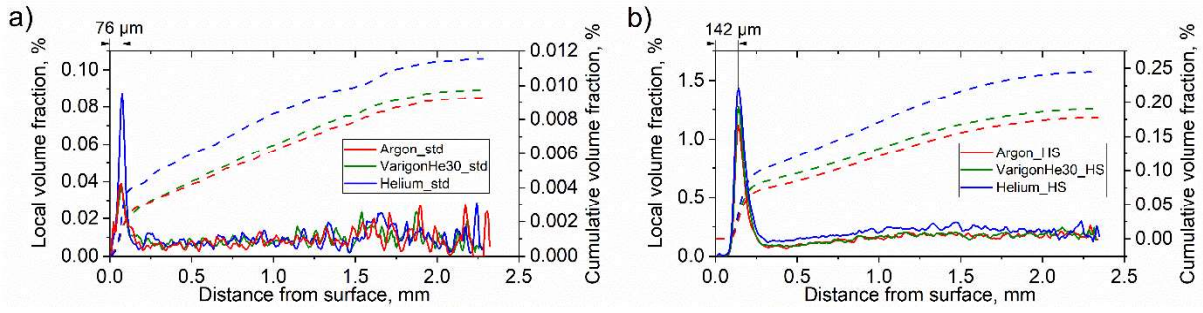


Figure 25: XCT results highlighting increased pore volume fraction close to the sample's edge under helium compared to argon and VarigonHe30 for (a) standard laser parameters and (b) increased scanning speed (from Paper IX).

From the enhanced melt pool stability under helium presented in the following section, effects on the thermal history and thus residual stresses (RS) developed during L-PBF using helium were expected. The measurement of subsurface RS using energy-dispersive diffraction of hard X-rays along the building direction of cuboids revealed that no differences on the scale of the part could be seen among argon, helium or the mixture. In addition, a significant reduction of the RS was achieved for the high aspect ratio design attributed to heat accumulation and in situ relief of RS. This RS reduction for the plate samples was almost three-fold regardless of the process atmosphere. However, some effects of helium were noted on the deflection of the cantilever structures partly removed from the baseplate. This point suggests that for large scanned surface, excessive RS can develop, highlighting the effect of the process gas on the part's thermal history.

9.3 Toward process stability and productivity increase

Reduction of hot spatters with helium

The shadowgraphy performed at Fraunhofer ILT confirmed the reduction of the generation of hot spatters for Ti-6Al-4V, by 60% with pure helium and by 30% with an argon-helium mixture, compared to standard argon, see Figure 26. This is consistent with complementary observations on EOS M290. Findings reveal that spatters cool approximately two times faster with helium compared to argon. This result is interesting to limit the high temperature oxidation of spatters. In addition, from Figure 26, the generated vapours were more displaced by the argon flow, which is harmful in the presented configuration since it leads to the laser shadowing. Additional analysis presented in Paper VIII revealed the faster expanding vapours in helium. In light of these findings, it was proposed that helium allows the rapid transport of vapours and spatters, which act as laser scattering objects, away from the laser spot.

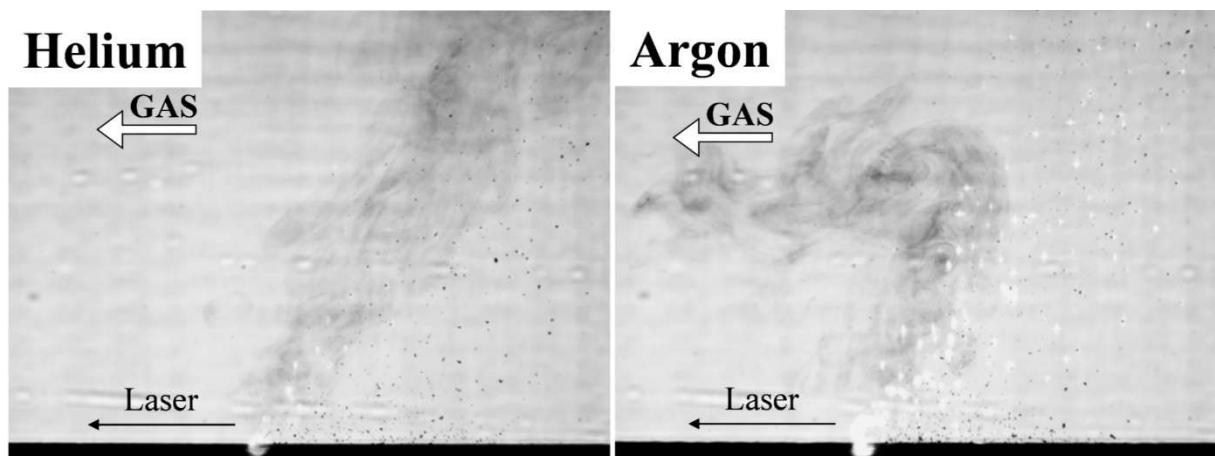


Figure 26: Reduction of Ti-6Al-4V spatter generation using helium, observed on a laboratory-scale L-PBF system (AconityMINI at Fraunhofer ILT, Germany).

Increased build rates with helium

Following the implementation of helium and its mixtures with argon for standard laser parameters, increased scanning speed for higher productivity was investigated. For 316L stainless steel the speed increase yielded a reduction of the cell size and the grain size factor, as well as a weaker texture. The helium-produced samples exhibited similar properties to that obtained with the traditionally used gases.

For Ti-6Al-4V, a doubled scanning speed (100% increase compared to standard) demonstrated the beneficial impact of the argon-helium mixtures on porosity. However, a 40% increase of the scanning speed did not lead to significant differences in porosity measured by laboratory XCT, which increased in a similar way to approximately 0.18% for argon and the mixture of 30% helium and the rest argon. For the material produced with a 40% increased scanning speed, no difference in mechanical response (Paper VII) and subsurface RS along the building direction (Paper IX) were measured, considering the different process gas. This finding suggests that the beneficial impact of helium^s addition on porosity may only be observed for excessive

build rates connected to porosity levels above 0.5%. Hence, this shows significant potential of helium and its mixes to reduce building time.

Material with this porosity level would most likely require post treatment, such as HIP, to be applicable to high-end industries' requirements, like in aerospace. Therefore, deeper analysis of the effect of different entrapped gas species in the porosity prior to HIP on the resulting porosity is of interest because of their different solubilities and diffusivities in the material and hence behaviour during HIPing. Preliminary results imply that high enough porosity, i.e. several percent, are required to possibly see a difference among different process gases, as HIP is efficient to achieve full density. In addition, residual oxygen in the process atmosphere appears to be an important variable since oxides and nitrides tend to accumulate in the vicinity of antecedent lack-of-fusion defects as highlighted for Alloy 718 in Figure 27. Their elongated morphology (see Figure 27b), promotes decohesion and critical crack initiation under fatigue loading.

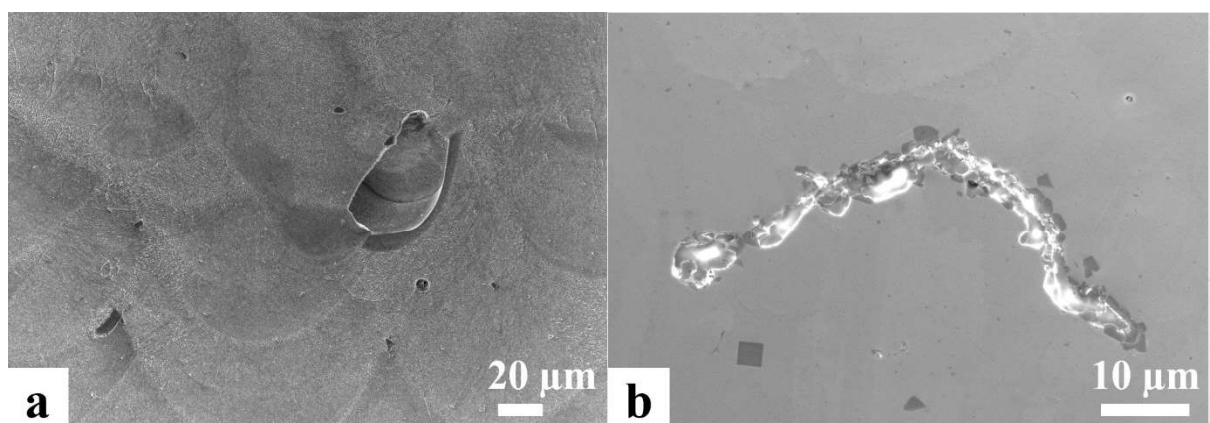


Figure 27: SEM micrographs displaying (a) the cross-section of an Alloy 718 cube built with high scanning speed under argon and uncontrolled residual oxygen content in the process atmosphere; (b) the accumulation of oxides and nitrides at a previous site of a lack-of-fusion porosity in a HIPed Alloy 718 sample.

CHAPTER 10

CONCLUSIONS

How does the purity of the L-PBF process atmosphere influence the process stability and material properties?

- The response to different purity levels in the L-PBF process atmosphere of the three studied materials, namely 316L, Alloy 718 and Ti6Al4V, is significantly different due to the difference in their composition and oxygen sensitivity.
- 316L stainless steel is a robust alloy to process by L-PBF that remains fully austenitic during processing. Its composition, microstructure, and mechanical properties are not significantly affected in the typical range of 1000 ppm O₂. 316L stainless steel tends to lose some oxygen during L-PBF processing, which is assumed to be transferred to more oxidized spatter particles and the process atmosphere.
- For higher than standard oxygen level of approximately 2000 ppm, the degradation of the used 316L stainless steel powder bed becomes more significant. The coverage of the particles by Cr-, Mn- and Si-rich particulates increases as the oxygen chemical potential in the processing atmosphere increases, resulting in the driving force for the powder/spatter oxidation.
- In a manner similar to 316L stainless steel, Alloy 718 exhibits consistent composition and microstructure when processed at low and intermediate oxygen levels (50 and 500 ppm O₂). Significant oxygen loss from the powder to the part was also reported.
- Alloy 718 spatters were distinguished between entrained particles from the powder bed and direct melt pool ejections. The analysis of their core microstructure highlighted a more rapid cooling of the direct melt pool ejections than the entrained particles, which preserve the microstructure of the virgin powder.
- The gradual reduction in residual oxygen in the process atmosphere significantly inhibits oxidation of Alloy 718 spatters, typically observed through the coverage and growth of Cr- and Al-rich oxide features.
- Ti-6Al-4V appeared to be the most sensitive alloy to L-PBF atmosphere purity and thus was significantly impacted by the L-PBF system characteristics, such as oxygen sensor types with electrochemical cells proving to be more reliable.
- An intermediate residual oxygen level (1000 ppm O₂ and above) was shown to cause lack-of-fusion porosity, oxygen pick-up, part discoloration and embrittlement. The extent of the formation of the mentioned defects is also closely related to process parameters and temperature and hence heat accumulation, which can be tuned by the interlayer time.
- Despite rather discrete oxide features forming on Ti-6Al-4V spatters, significant oxygen and nitrogen pick-up were measured.

How does the type of L-PBF process atmosphere influence the material properties?

- Both 316L stainless steel and Alloy 718, can be processed under nitrogen without significant composition or microstructural changes being observed. The rather limited nitrogen pick-up in both cases was attributed to the rapid cooling limiting the kinetics of nitrogen dissolution. For Alloy 718, a slightly higher nitrogen content was measured in produced samples under nitrogen compared to argon.
- Helium has been successfully implemented as a process gas for 316L stainless steel and Ti-6Al-4V, yielding high density and mechanical properties comparable to those obtained with standard argon. Slightly reduced cell size was reported for 316L stainless steel samples produced under helium compared to their argon and nitrogen counterparts.
- Finally, helium and its mixtures did not introduce additional residual stresses in Ti-6Al-4V plate and cuboid geometries. For larger components of more complex design, such as cantilever, more important deformations following the direct removal from the baseplate were measured and attributed to enhanced convection heat transfer by helium.

How does the type of L-PBF process atmosphere influence the process stability and productivity?

- Helium and argon-helium mixtures were identified as a possible solution to reduce Ti-6Al-4V spatter generation as observed by the naked eye and later confirmed with a shadowgraphy experiment. Helium additions were also granting faster cooling of hot spatters.
- For increased build rates, at about 40% for Ti-6Al-4V, by increasing scanning speed, the results highlight that helium can be implemented as a process gas and yields similar material properties as with argon.
- For high build rates leading to productivity increases of about 70%, an increase in porosity to above 0.5% was observed, and helium and argon-helium mixtures appeared to be of interest to reduce porosity compared to argon.

To conclude the results of this study, Figure 28 summarizes the findings connected to oxygen and nitrogen exchanges during L-PBF of 316L stainless steel, Alloy 718 and Ti-6Al-4V, and proposes a model to interpret the effect of helium addition to the process gas on the laser-powder bed interaction.

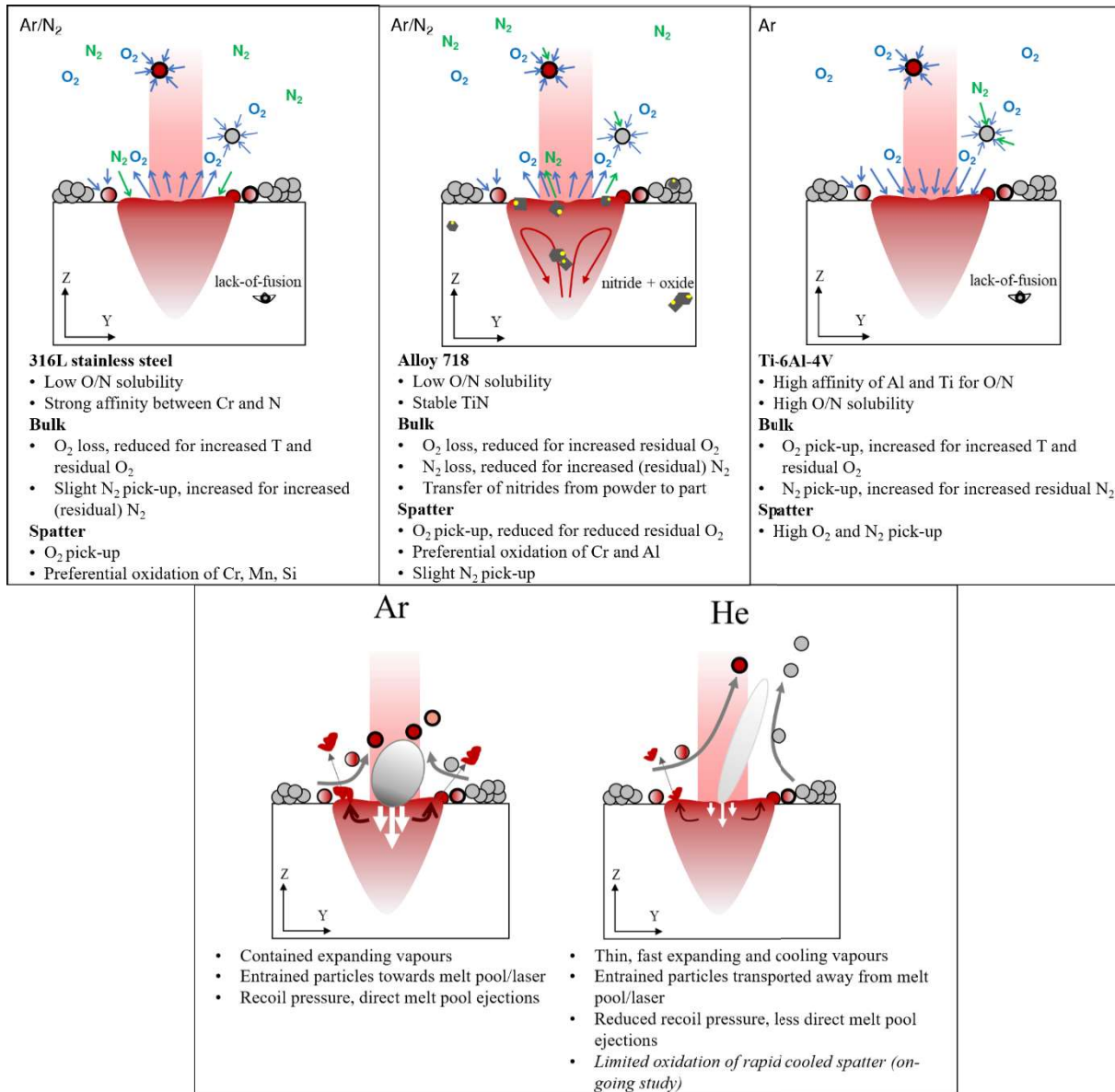


Figure 28: Summarizing illustrations of findings connected to oxygen and nitrogen exchange during L-PBF and model of the effect of helium addition on the melt pool dynamics.

CHAPTER 11

OUTLOOK

New aspects have emerged in the area of process gases for L-PBF based on the results obtained during this thesis work and would be interesting to explore. Despite the observed robustness of L-PBF processing of 316L stainless steel using nitrogen atmosphere and typical oxygen levels, this study focused primarily on static mechanical properties, and hence the effect of process gas on a broader range of mechanical properties with focus on dynamic properties should be studied. In addition, corrosion behaviour of the material produced under nitrogen should reveal the possible effect of the characteristic of the L-PBF microstructure (anisotropy, potential presence of chromium nitrides, etc.) on corrosion properties. In parallel, in light of recent published work related to both liquid metal deposition¹¹⁴ and PBF^{51,65}, there might be interest in developing oxide-dispersion-strengthened and nitride-dispersion-strengthened steel components using a combination of tailored feedstock composition, e.g. Si/Ti to form nitrides and Y/Al to form oxides, and process atmosphere, e.g. additions of CO₂, H₂.

Considering the use of nitrogen to process Alloy 718, the mechanical properties of parts produced as such should be evaluated at room and service temperatures and compared to standard requirements of the alloy. Studying the effect of as-received oxygen levels in the powder feedstock in detail, especially on the low range, would also be of interest. In addition, future research might investigate the further use of nitrogen compared to standard argon in the context of a more complex process chain, including heat treatment and HIP. The promising results connected to oxidation mitigation of spatter by reducing residual oxygen could, through experiments, be extended to other Ni-base superalloys, also rich in strong oxide formers, such as B and Zr for IN-738LC¹¹⁵ and susceptible to cracking.

Modelling of the gas-laser-powder interaction for the newly investigated atmospheres and considering the thermal properties of the gas can be helpful in improving understanding of the reduction of spatter generation with addition of helium. In parallel, the rapid development and implementation of new monitoring devices, as for example the thermionic emission detection implemented by DePond et al.¹¹⁶ is promising to better grasp the dynamics of the gas-laser-powder interaction.

Completing the work connected to productivity and stability increase by investigating increased layer thickness is also recommended. In this work only the increased scanning speed approach was proposed. Increasing layer thickness has proven to be an efficient method to reduce build time, however it does create increased interaction volume of powder particles, and

thus comparing the behaviour of helium to the more standard gas under such conditions is of interest.

A work in progress between Chalmers, Linde and the Paul Scherrer Institute (Villingen, Switzerland) focuses on the effect of helium in the process gas and gas speed on the cooling rates experienced by Ti-6Al-4V during L-PBF. This research is possible with the in-house designed L-PBF system allowing for *in operando* X-ray diffraction at a synchrotron beamline. These investigations received support from Vinnova (Ulrica project: DNr 2019-05272). The early examination of the produced samples reveal a promising lower average surface roughness, which is consistent with the reduced amount of spatter with helium reported in this thesis.

Finally, the newest results generated at the end of 2020 demonstrate that mixtures of only 30% helium, with the rest argon, to process Alloy 718 also present great potential to limit the generation of spatter for bulk parts and lattice structures compared to standard argon, using the ExposureOT monitoring of the EOS M290 system. Therefore, on a more general note, toward the end of this PhD work, many possibilities and opportunities arose, highlighting that we are at the beginning of the journey to develop tailored process gases for L-PBF.

ACKNOWLEDGEMENTS

I would like to express sincere thanks to my supervisor Eduard Hryha, for his encouragement, efforts and guidance. I also express my gratitude to my co-supervisors Pierre Forêt for his support and motivation in the realisation of this work, and Lars Nyborg for his assistance, feedback and discussions. Thank you for granting me the opportunity to embark on this PhD journey. I feel lucky and grateful for the people I met and the places I had the chance to visit.

Gratitude goes to Linde GmbH, the Centre for Additive Manufacturing – Metal (CAM²) and Innoglobe supported by Vinnova for providing a framework for this thesis.

I am grateful to all my co-authors and colleagues for the collaborations, learnings and discussions.

Special thanks are addressed to Sophie Dubiez-Le Goff. I am glad we could keep such close contact after my move to Sweden. Thanks for the phone calls, your patience, support and generosity.

From the Bavarian office, special thanks go to Kai, Tanja, Anja, Dominik, Thomas, Siegi, Sebastian, Andrés, Saravana, Jens, Nakhleh, Anja, Toan, Micha, for their patience and support. My regards also go to Christoph Laumen for welcoming me in Unterschleissheim, and Edward Fang for his guidance in my trip to Beijing. Special thanks are extended to the Swedish Linde office and particularly to Bo Williamsson, Bartek Kaplan and Sören Wiberg.

The Chalmers office has also been a very cheerful place to work at and I am grateful to all my colleagues from the Department of Industrial and Materials Science. Many thanks for the nice AM discussions to Alex, Dmitri, William, Marie, Ahmad, Zhuoer, Fiona, Anok, Masoud, Mahesh, Hans, Bala, Bharat, Shaafi, Claudia, Alberto, Eric, Mikael. Many thanks to my officemate Antonio, for his patience and support. Also special regards go to Philipp, Casey, and all fika partners for their contribution to this nice atmosphere.

Roger Sagdahl, Yiming Yao, Eric Tam, Yu Cao and Håkan Millqvist are specially thanked for their availability and strong support.

I would also like to thank Andreas Markström from ThermoCalc, Sven Bengtsson, Sigurd Berg and Björn Skärman from Höganäs AB, Ola Lyckfeldt and Jonas Holmberg from RISE, Johannes Gårdstam from Quintus, Tatiana Mishurova and Giovanni Bruno from the Bundesanstalt für Materialforschung und-prüfung, Tobias Pichler from Fraunhofer ILT and Birk Hoppe from SLM Solutions.

I am grateful to my friends for their support in this journey and the happy times together.

Special thanks to Stefan, for your patience, support, care and encouragement.

J'adresse enfin un remerciement tout particulier à ma famille, mes parents et mes frères, pour m'avoir encouragée dans cette aventure et aidée à surmonter les difficultés et les moments de doute.

REFERENCES

1. ASTM International. ISO/ASTM 52900: Standard Terminology for Additive Manufacturing – General Principles – Terminology. *ASTM Int.* **1**, 1–9 (2015).
2. AMPOWER GmbH & Co. KG. *AMPower Report 2020*. (2020).
3. European Committee for Standardization. ISO 17296-2:2016 - Additive manufacturing – General principles – Part 2: Overview of process categories and feedstock. in (2016).
4. Bojestig, E., Cao, Y. & Nyborg, L. Surface chemical analysis of copper powder used in additive manufacturing. *Surf. Interface Anal.* **52**, 1104–1110 (2020).
5. EOS GmbH. Case studies for Industrial 3D Printing. Available at: <https://www.eos.info/en/3d-printing-examples-applications>.
6. Longhitano, G. A., Nunes, G. B., Candido, G. & da Silva, J. V. L. The role of 3D printing during COVID-19 pandemic: a review. *Prog. Addit. Manuf.* (2020). doi:10.1007/s40964-020-00159-x
7. Inc., G. Technology Research Gartner Inc. Available at: www.gartner.com.
8. Ge, Q. *et al.* Multimaterial 4D Printing with Tailorable Shape Memory Polymers. *Sci. Rep.* **6**, 1–11 (2016).
9. Markstedt, K. *et al.* 3D bioprinting human chondrocytes with nanocellulose-alginate bioink for cartilage tissue engineering applications. *Biomacromolecules* **16**, 1489–1496 (2015).
10. Linde Gas. ADDvance® O₂ precision – AM gas atmosphere control. Available at: https://www.linde-gas.com/en/processes/additive_manufacturing/3d_printing/addvance/index.html. (Accessed: 25th January 2021)
11. Trapp, J., Rubenchik, A. M., Guss, G. & Matthews, M. J. In situ absorptivity measurements of metallic powders during laser powder-bed fusion additive manufacturing. *Appl. Mater. Today* **9**, 341–349 (2017).
12. Li, Z., Zeze, M. & Mukai, K. Surface Tension and Wettability of Liquid Fe-16mass%Cr-S Alloy with Alumina. *Mater. Trans. JIM* **44**, 2108–2113 (2003).
13. Li, Z., Mukai, K., Zeze, M. & Mills, K. Determination of the surface tension of liquid stainless steel. *J. Mater. Sci.* **0**, 2191–2195 (2005).
14. Shcheglov, P. *Study of Vapour-Plasma Plume during High Power Fiber Laser Beam Influence on Metals*. (2012).
15. Bidare, P., Bitharas, I., Ward, R. M., Attallah, M. M. & Moore, A. J. Laser powder bed fusion in high-pressure atmospheres. *Int. J. Adv. Manuf. Technol.* 1–13 (2018). doi:10.1007/s00170-018-2495-7
16. Bidare, P., Bitharas, I., Ward, R. M., Attallah, M. M. & Moore, A. J. Fluid and particle dynamics in laser powder bed fusion. *Acta Mater.* **142**, 107–120 (2018).
17. Ly, S., Rubenchik, A. M., Khairallah, S. A., Guss, G. & Manyalibo, J. Metal vapor micro-jet controls material redistribution in laser powder bed fusion additive

- manufacturing. 1–12 (2017). doi:10.1038/s41598-017-04237-z
18. Calta, N. P. *et al.* Cooling dynamics of two titanium alloys during laser powder bed fusion probed with in situ X-ray imaging and diffraction. *Mater. Des.* **195**, 108987 (2020).
 19. Hoppe, B. & Enk, S. Schlieren- and shadowgraphy for visualization of the shielding gas dynamics in laser powder bed fusion. in *Rapid.Tech* 197–210 (2019).
 20. Hocine, S. *et al.* In operando X-ray diffraction during laser 3D printing. *Mater. Today* 1–12 (2019). doi:10.1016/j.mattod.2019.10.001
 21. Fuchs, L. & Eischer, C. In-process monitoring systems for metal additive manufacturing.
 22. Mercelis, P. & Kruth, J. Residual stresses in selective laser sintering and selective laser melting. **5**, 254–265 (2006).
 23. Bartlett, J. L. & Li, X. An overview of residual stresses in metal powder bed fusion. *Addit. Manuf.* **27**, 131–149 (2019).
 24. Dieter, G. Mechanical metallurgy. (1961).
 25. Mishurova, T. *et al.* An assessment of subsurface residual stress analysis in SLM Ti-6Al-4V. *Materials (Basel)*. **10**, (2017).
 26. Parry, L., Ashcroft, I. A. & Wildman, R. D. Understanding the effect of laser scan strategy on residual stress in selective laser melting through thermo-mechanical simulation. *Addit. Manuf.* **12**, 1–15 (2016).
 27. Law, J. *A dictionary of business and management*. (Oxford University Press, 2009). doi:10.1093/acref/9780199234899.001.0001
 28. Cambridge University Press. Dictionary Cambridge advanced learner's and thesaurus. Available at: <https://dictionary.cambridge.org/fr/dictionnaire/anglais/productivity>. (Accessed: 5th August 2020)
 29. Yin, J. *et al.* High-power laser-matter interaction during laser powder bed fusion. *Addit. Manuf.* **29**, 100778 (2019).
 30. EOS GmbH. Datasheet: EOS M 300 Series.
 31. GE Additive. Datasheet: Concept Laser X Line 2000R.
 32. DMG MORI. Brochure: DMG MORI LASERTEC 4300 3D hybrid. (2020).
 33. Siemens AG. Industrialization of Additive Manufacturing. (2017).
 34. Seifi, M. Standards for additive manufacturing: the latest developments by ASTM International's Dr Mohsen Seifi. *TCT Magazine* (2020).
 35. Chalmers University of Technology. CAM2 Centre for Additive Manufacturing - Metal: Education. Available at: <https://www.chalmers.se/en/centres/cam2/education/Pages/default.aspx>. (Accessed: 5th August 2020)
 36. Almqvist, E. *History of Industrial Gases*. (Springer US, 2003). doi:10.1007/978-1-4615-0197-8
 37. Hryha, E., Dudrova, E. & Nyborg, L. On-line control of processing atmospheres for

- proper sintering of oxidation-sensitive PM steels. *J. Mater. Process. Technol.* **212**, 977–987 (2012).
38. Hauser, C., Childs, T. H. C., Dalgarno, K. W. & Eane, R. B. Atmospheric Control during Direct Selective Laser Sintering of Stainless Steel 314S Powder. *10th Solid Free. Fabr. Symp.* 265–272 (1999).
 39. Li, R., Liu, J., Shi, Y., Wang, L. & Jiang, W. Balling behavior of stainless steel and nickel powder during selective laser melting process. *Int. J. Adv. Manuf. Technol.* **59**, 1025–1035 (2012).
 40. Dietrich, K., Diller, J., Dubiez-le Goff, S., Bauer, D. & Forêt, P. The influence of oxygen on the chemical composition and mechanical properties of Ti-6Al-4V during laser powder bed fusion (L-PBF). *L-PBF*. **32**, (2020).
 41. Pauzon, C., Hryha, E., Forêt, P. & Nyborg, L. Effect of argon and nitrogen atmospheres on the properties of stainless steel 316L parts produced by laser-powder bed fusion. *Mater. Des.* 107873 (2019). doi:10.1016/j.matdes.2019.107873
 42. Reijonen, J., Revuelta, A., Riipinen, T., Ruusuvuori, K. & Puukko, P. On the effect of shielding gas flow on porosity and melt pool geometry in laser powder bed fusion additive manufacturing. *Addit. Manuf.* **32**, 101030 (2020).
 43. Ferrar, B., Mullen, L., Jones, E., Stamp, R. & Sutcliffe, C. J. Gas flow effects on selective laser melting (SLM) manufacturing performance. *J. Mater. Process. Technol.* **212**, 355–364 (2012).
 44. Schniedenharn, M. & Schleifenbaum, J. H. On the Correlation of the Shielding Gas Flow in L-PBF Machines with Part Density. in *DDMC2018 Fraunhofer Direct Digital Manufacturing Conference* 1–7 (2018).
 45. Chen, Z. & Chen, Z. Surface roughness of Selective Laser Melted Ti-6Al-4V alloy. (Monash University, 2018).
 46. Anwar, A. Bin & Pham, Q. C. Selective laser melting of AlSi10Mg: Effects of scan direction, part placement and inert gas flow velocity on tensile strength. *J. Mater. Process. Technol.* **240**, 388–396 (2017).
 47. Bergman, T. L. & Lavine, A. S. *Fundamentals of heat and mass transfer - Eight edition*. (2017).
 48. Dai, D. & Gu, D. Effect of metal vaporization behavior on keyhole-mode surface morphology of selective laser melted composites using different protective atmospheres. *Appl. Surf. Sci.* **355**, 310–319 (2015).
 49. Wang, X. J., Zhang, L. C., Fang, M. H. & Sercombe, T. B. The effect of atmosphere on the structure and properties of a selective laser melted Al-12Si alloy. *Mater. Sci. Eng. A* **597**, 370–375 (2014).
 50. Traore, S. *et al.* Influence of gas atmosphere (Ar or He) on the laser powder bed fusion of a Ni-based alloy. *J. Mater. Process. Tech.* **288**, 116851 (2021).
 51. Haines, M. P., Peter, N. J., Babu, S. S. & Jägle, E. A. In-situ synthesis of oxides by reactive process atmospheres during L-PBF of stainless steel. *Addit. Manuf.* 101178 (2020). doi:10.1016/j.addma.2020.101178
 52. ASTM International. F3184-16 Standard Specification for Additive Manufacturing

Stainless Steel Alloy (UNS S31603) with Powder Bed Fusion. in (ed. ASTM International, 2016) **i**, 1–9 (2020).

53. Wang, Y. M. *et al.* Additively manufactured hierarchical stainless steels with high strength and ductility. *Nat. Mater.* **17**, (2018).
54. Wang, D., Song, C., Yang, Y. & Bai, Y. Investigation of crystal growth mechanism during selective laser melting and mechanical property characterization of 316L stainless steel parts. *Mater. Des.* **100**, 291–299 (2016).
55. Sun, Z., Tan, X., Tor, S. B. & Yeong, W. Y. Selective laser melting of stainless steel 316L with low porosity and high build rates. *Mater. Des.* **104**, 197–204 (2016).
56. Prashanth, K. G. & Eckert, J. Formation of metastable cellular microstructures in selective laser melted alloys. *J. Alloys Compd.* **707**, 27–34 (2017).
57. Sun, Z., Tan, X., Tor, S. B. & Chua, C. K. Simultaneously enhanced strength and ductility for 3D-printed stainless steel 316L by selective laser melting. *NPG Asia Mater.* **10**, 127–136 (2018).
58. Leicht, A., Yu, C. H., Luzin, V., Klement, U. & Hryha, E. Effect of scan rotation on the microstructure development and mechanical properties of 316L parts produced by laser powder bed fusion. *Mater. Charact.* **163**, 2–10 (2020).
59. Leicht, A., Rashidi, M., Klement, U. & Hryha, E. Effect of process parameters on the microstructure, tensile strength and productivity of 316L parts produced by laser powder bed fusion. *Mater. Charact.* 110016 (2019). doi:10.1016/j.matchar.2019.110016
60. Rawers, J. C., Frisk, K. & Govier, D. Nitrogen in pressure-diffused powder iron alloys. *177*, 243–251 (1994).
61. Somers, M. A. J., Christiansen, T. L. & Winther, G. Expanded austenite ; from fundamental understanding to predicting composition- and stress-depth profiles. (2018).
62. Kitchener, J. A., Bockris, J. O. M., Gleiser, M. & Evans, J. W. The solubility of oxygen in gamma iron. *Acta Metall.* **1**, 93–101 (1953).
63. Cooper, A. J., Brayshaw, W. J. & Sherry, A. H. Tensile Fracture Behavior of 316L Austenitic Stainless Steel Manufactured by Hot Isostatic Pressing. *Metall. Mater. Trans. A* **49**, 1579–1591 (2018).
64. Lou, X., Andresen, P. L. & Rebak, R. B. Oxide inclusions in laser additive manufactured stainless steel and their effects on impact toughness and stress corrosion cracking behavior. *J. Nucl. Mater.* **499**, 182–190 (2018).
65. Riabov, D. The effects of morphology and surface oxidation of stainless steel powder in laser based-powder bed fusion. (Chalmers University of Technology, 2020).
66. Zhong, Y. *et al.* Oxide dispersion strengthened stainless steel 316L with superior strength and ductility by selective laser melting. *J. Mater. Sci. Technol.* **42**, 97–105 (2020).
67. Rafi, H. K., Pal, D., Patil, N., Starr, T. L. & Stucker, B. E. Microstructure and Mechanical Behavior of 17-4 Precipitation Hardenable Steel Processed by Selective Laser Melting. *23*, 4421–4428 (2014).
68. Cheruvathur, S., Lass, E. A. & Campbell, C. E. Additive Manufacturing of 17-4 PH Stainless Steel : Post-processing Heat Treatment to Achieve Uniform Reproducible

- Microstructure. **68**, 930–942 (2016).
69. Reed, R. C. *The superalloys: fundamentals and applications*. (Cambridge University Press, 2009).
 70. Brooks, J. W. & Bridges, P. J. Metallurgical Stability of Inconel Alloy 718. 33–42 (1988).
 71. Cozar, R. & Pineau, A. Morphology of gamma prime an gamma double prime precipitates and thermal stability of Inconel 718 type alloys. *Metall. Trans.* **4**, 47–59 (1973).
 72. Zhang, D., Niu, W., Cao, X. & Liu, Z. Effect of standard heat treatment on the microstructure and mechanical properties of selective laser melting manufactured Inconel. *Mater. Sci. Eng. A* **644**, 32–40 (2015).
 73. Committee, A. F. C. H. R. A. AMS 5662. in (SAE International, 2019). doi:<https://doi.org/10.4271/AMS5662M>
 74. Deng, D., Peng, R. L., Brodin, H. & Moverare, J. Microstructure and mechanical properties of Inconel 718 produced by selective laser melting: Sample orientation dependence and effects of post heat treatments. *Mater. Sci. Eng. A* **713**, 294–306 (2018).
 75. Wang, X. & Chou, K. Effects of thermal cycles on the microstructure evolution of Inconel 718 during selective laser melting process. *Addit. Manuf.* **18**, 1–14 (2017).
 76. Zhao, J., Hung, F. & Lui, T. Microstructure and tensile fracture behavior of three-stage heat treated inconel 718 alloy produced via laser powder bed fusion process. *Integr. Med. Res.* **9**, 3357–3367
 77. Rao, G. A., Srinivas, M. & Sarma, D. S. Effect of oxygen content of powder on microstructure and mechanical properties of hot isostatically pressed superalloy Inconel 718. *Mater. Sci. Eng. A* **435–436**, 84–99 (2006).
 78. Gasper, A. N. D. *et al.* Spatter and oxide formation in laser powder bed fusion of Inconel 718. *Addit. Manuf.* **24**, 446–456 (2018).
 79. Cockcroft, S. L., Degawa, T., Mitchell, A., Tripp, D. W. & Schmalz, A. Inclusion Precipitation in Superalloys. 577–586 (2012). doi:[10.7449/1992/superalloys_1992_577_586](https://doi.org/10.7449/1992/superalloys_1992_577_586)
 80. Mitchell, A., Schmalz, A. J., Schvezov, C. & Cockcroft, S. L. The Precipitation of Primary Carbides in Alloy 718. in *Superalloys 718, 625, 706 and Various Derivatives* 65–78 (The Minerals, Metals & Materials Society, 1994). doi:[10.7449/1994/superalloys_1994_65_78](https://doi.org/10.7449/1994/superalloys_1994_65_78)
 81. Haynes, W. M., Lide, D. R. & Bruno, T. J. *CRC handbook of chemistry and physics*. (CRC Press).
 82. Ahmed, T. & Rack, H. J. Phase transformations during cooling in $\alpha + \beta$ titanium alloys. *Mater. Sci. Eng. A* **243**, 206–211 (1998).
 83. ASTM-International. ASTM F2924-14: Standard Specification for Additive Manufacturing Titanium-6 Aluminum-4 Vanadium with Powder Bed Fusion. 1–9 (2017). doi:[10.1520/F2924-14.2](https://doi.org/10.1520/F2924-14.2)
 84. Pantawane, M. V, Dasari, S., Mantri, S. A., Banerjee, R. & Dahotre, N. B. Rapid thermokinetics driven nanoscale vanadium clustering within martensite laths in laser

- powder bed fused additively manufactured Ti6Al4V. *Mater. Res. Lett.* **8**, 383–389 (2020).
- 85. Yang, J. *et al.* Formation and control of martensite in Ti-6Al-4V alloy produced by selective laser melting. *Mater. Des.* **108**, 308–318 (2016).
 - 86. EOS GmbH. Material data sheet EOS Titanium Ti64 Material data sheet Technical data. **49**, 1–5 (2014).
 - 87. Yu, Q. *et al.* Origin of dramatic oxygen solute strengthening effect in titanium. *Science (80-.)* **347**, 635–639 (2015).
 - 88. Lütjering, G. & Williams, J. C. Titanium : Engineering Materials and Processes. *Ed. SPRINGER second edi*, 1–442 (2007).
 - 89. Barba, D. *et al.* On the size and orientation effect in additive manufactured Ti-6Al-4V. *Mater. Des.* **186**, 108235 (2020).
 - 90. Velasco-Castro, M., Hernández-Nava, E., Figueroa, I. A., Todd, I. & Goodall, R. The effect of oxygen pickup during selective laser melting on the microstructure and mechanical properties of Ti–6Al–4V lattices. *Heliyon* **5**, (2019).
 - 91. Chen, H. *et al.* Powder-spreading mechanisms in powder-bed-based additive manufacturing : Experiments and computational modeling. *Acta Mater.* **179**, 158–171 (2019).
 - 92. Sims, C. T., Stoloff, N. S. & Hagel, W. C. *Superalloys II: High-temperature materials for aerospace and industrial power.* (1987).
 - 93. Balachandramurthi, A. R. *Fatigue Properties of Additively Manufactured Alloy 718.* (2018).
 - 94. Ramanathan, A., Moverare, J., Dixit, N., Deng, D. & Pederson, R. Microstructural influence on fatigue crack propagation during high cycle fatigue testing of additively manufactured Alloy 718. *Mater. Charact.* **149**, 82–94 (2019).
 - 95. Sundaram, M. V. *Novel approaches for achieving full density powder metallurgy steels.* (2019).
 - 96. Rashidi, M., Liljestrand, F., Nyborg, L. & Hryha, E. Porosity closure using hot isostatic pressing and re-opening of porosity during subsequent heat treatment of additively manufactured IN718. in *Euromat* (2019).
 - 97. Tammas-Williams, S. *et al.* XCT analysis of the influence of melt strategies on defect population in Ti-6Al-4V components manufactured by Selective Electron Beam Melting. *Mater. Charact.* **102**, 47–61 (2015).
 - 98. Weingarten, C. *et al.* Formation and reduction of hydrogen porosity during selective laser melting of AlSi10Mg. *J. Mater. Process. Tech.* **221**, 112–120 (2015).
 - 99. Martin, A. A. *et al.* Dynamics of pore formation during laser powder bed fusion additive manufacturing. *Nat. Commun.* 1–10 (2019). doi:10.1038/s41467-019-10009-2
 - 100. Cunningham, R., Zhao, C., Parab, N. & Kantzios, C. Keyhole threshold and morphology in laser melting revealed by ultrahigh-speed x-ray imaging. **852**, 849–852 (2019).
 - 101. Clifford, A. A., Fleeter, R., Kestin, J. & Wakeham, W. A. Thermal conductivity of some mixtures of monatomic gases at room temperature and at pressure up to 15 MPa. *Phys.*

A Stat. Mech. its Appl. **98**, 467–490 (1979).

102. Vernon-Parry, K. D. Scanning Electron Microscopy : An introduction. *III-Vs Rev.* **13**, 40–44 (2000).
103. Cunningham, R., Narra, S. P., Montgomery, C., Beuth, J. & Rollett, A. D. Synchrotron-Based X-ray Microtomography Characterization of the Effect of Processing Variables on Porosity Formation in Laser Power-Bed Additive Manufacturing of Ti-6Al-4V. **69**, 2–7 (2017).
104. Kastner, J., Harrer, B., Requena, G. & Brunke, O. A comparative study of high resolution cone beam X-ray tomography and synchrotron tomography applied to Fe- and Al-alloys. *NDT E Int.* **43**, 599–605 (2010).
105. Cnudde, V. & Boone, M. N. Earth-Science Reviews High-resolution X-ray computed tomography in geosciences : A review of the current technology and applications. *Earth Sci. Rev.* **123**, 1–17 (2013).
106. ASTM- International. ASTM E23-16b: Standard Test Methods for Notched Bar Impact Testing of Metallic Materials. *ASTM B. Stand.* **i**, 1–26 (2016).
107. ASTM-International. ASTM B925-15: Standard Practices for Production and Preparation of Powder Metallurgy (P / M) Test. **03**, 1–15 (2003).
108. ASTM-International. ASTM E8/E8M-15a: Standard Test Methods for Tension Testing of Metallic Materials. 1–29 (2015). doi:10.1520/E0008
109. DIN 50125 - Testing of metallic materials - Tensile test pieces.
110. DIN EN ISO 6892-1:2016 - Metallic materials - Tensile testing - Part 1: Method of test at room temperature. (2017).
111. Mishurova, T., Artzt, K., Haubrich, J., Requena, G. & Bruno, G. Exploring the correlation between subsurface residual stresses and manufacturing parameters in laser powder bed fused ti-6al-4v. *Metals (Basel)*. **9**, (2019).
112. Watts, J. F. & Wolstenholme, J. *An introduction to surface analysis by XPS and AES*. (2003).
113. Tinevez, J. Y. *et al.* TrackMate: An open and extensible platform for single-particle tracking. *Methods* **115**, 80–90 (2017).
114. Springer, H. *et al.* Efficient additive manufacturing production of oxide- and nitride-dispersion-strengthened materials through atmospheric reactions in liquid metal deposition. *Mater. Des.* **111**, 60–69 (2016).
115. Gruber, H. *Powder bed fusion processing of Ni-base superalloys*. Thesis (2020).
116. DePond, P. J. *et al.* Laser-metal interaction dynamics during additive manufacturing resolved by detection of thermally-induced electron emission. *Commun. Mater.* **1**, 1–10 (2020).